JEM Journal of Experimental Medicine

ARTICLE

Impaired immune response drives age-dependent severity of COVID-19

Julius Beer[1], Stefania Crotta[2], Angele Breithaupt[3], Annette Ohnemus[1], Jan Becker[1], Benedikt Sachs[1], Lisa Kern[1], Miriam Llorian[4], Nadine Ebert[5,6], Fabien Labroussaa[6,7], Tran Thi Nhu Thao[5,6,8], Bettina Salome Trueeb[6,7], Joerg Jores[6,7], Volker Thiel[5,6,9], Martin Beer[10], Jonas Fuchs[1], Georg Kochs[1], Andreas Wack[2], Martin Schwemmle[1,11], and Daniel Schnepf[1]

Severity of COVID-19 shows an extraordinary correlation with increasing age. We generated a mouse model for severe COVID-19 and show that the age-dependent disease severity is caused by the disruption of a timely and well-coordinated innate and adaptive immune response due to impaired interferon (IFN) immunity. Aggravated disease in aged mice was characterized by a diminished IFN-γ response and excessive virus replication. Accordingly, adult IFN-γ receptor-deficient mice phenocopied the age-related disease severity, and supplementation of IFN-γ reversed the increased disease susceptibility of aged mice. Further, we show that therapeutic treatment with IFN-λ in adults and a combinatorial treatment with IFN-γ and IFN-λ in aged *Ifnar1*$^{-/-}$ mice was highly efficient in protecting against severe disease. Our findings provide an explanation for the age-dependent disease severity and clarify the nonredundant antiviral functions of type I, II, and III IFNs during SARS-CoV-2 infection in an age-dependent manner. Our data suggest that highly vulnerable individuals could benefit from immunotherapy combining IFN-γ and IFN-λ.

Introduction

Within two and a half years since its introduction into the human population, SARS-CoV-2 has caused close to 600 million confirmed cases of COVID-19 leading to about 6.4 million deaths globally as of July 2022 (WHO, 2022). Interestingly, the burden of severe disease and mortality is not equally distributed across age groups and shows an extraordinary log-linear correlation with increasing age for individuals older than 30 yr (O'Driscoll et al., 2021). To enable the rational design of effective therapeutics and prevention strategies for vulnerable groups, a better understanding of disease-causing mechanisms is urgently needed.

One common hallmark of severe COVID-19 and advanced age is a diminished and delayed innate immune response affecting the timely production of IFNs (Bartleson et al., 2021; Shaw et al., 2013; Channappanavar and Perlman, 2020; Wong and Perlman, 2022). Type I, II, and III IFNs, also called IFN-α/β, IFN-γ, and IFN-λ, respectively, are known antiviral cytokines that are rapidly produced by the host upon recognition of viral material. IFNs orchestrate an immediate cell-intrinsic innate immune response by upregulating expression levels of interferon-stimulated genes (ISGs) and initiate the subsequent adaptive immune response by the recruitment and activation of immune cells (Ye et al., 2019b; Akamatsu et al., 2021; Paludan and Mogensen, 2022; Park and Iwasaki, 2020). The delayed and diminished IFN response in severe COVID-19 is associated with a late and dysregulated inflammatory gene expression signature (Park and Iwasaki, 2020; Wong and Perlman, 2022; Galani et al., 2021; Hadjadj et al., 2020), possibly due to enhanced tissue damage caused by an insufficient control of virus replication. The clinical relevance of a well-functioning IFN response was emphasized by the finding that 3.5% of patients with life-threatening COVID-19 had genetic defects in genes involved in virus recognition, IFN production, and signaling, including *TLR3*, *TBK1*, *IRF3*, *IRF7*, *IFNAR1*, and *IFNAR2* (Zhang et al., 2020). In addition, type I IFN neutralizing antibodies were detected in another 10% of critically ill COVID-19 patients with a tendency of increased frequency in the elderly (Bastard et al., 2020). Even though clinical penetrance of neutralizing antibodies against

[1]Institute of Virology, Medical Center University of Freiburg, Freiburg, Germany; [2]Immunoregulation Laboratory, The Francis Crick Institute, London, UK; [3]Department of Experimental Animal Facilities and Biorisk Management, Friedrich-Loeffler-Institut, Greifswald-Insel Riems, Germany; [4]Bioinformatics and Biostatistics, The Francis Crick Institute, London, UK; [5]Institute of Virology and Immunology, Bern, Switzerland; [6]Department of Infectious Diseases and Pathobiology, Vetsuisse Faculty, University of Bern, Bern, Switzerland; [7]Institute of Veterinary Bacteriology, Vetsuisse Faculty, University of Bern, Bern, Switzerland; [8]Graduate School for Biomedical Science, University of Bern, Bern, Switzerland; [9]Multidisciplinary Center for Infectious Diseases, University of Bern, Switzerland; [10]Institute of Diagnostic Virology, Friedrich-Loeffler-Institut, Greifswald-Insel Riems, Germany; [11]Faculty of Medicine, University of Freiburg, Freiburg, Germany.

Correspondence to Daniel Schnepf: daniel.schnepf@uniklinik-freiburg.de; Martin Schwemmle: martin.schwemmle@uniklinik-freiburg.de.

type I IFNs for severe COVID-19 is not complete (Meisel et al., 2021), they may promote lethal disease progression in up to 20% of deaths caused by SARS-CoV-2 infection (Bastard et al., 2021). The markedly lower risk of children developing severe COVID-19 on the other hand correlates with an increased basal expression level of the pattern-recognition receptors (PRRs) MDA5 and RIG-I, leading to a stronger innate antiviral immune response upon SARS-CoV-2 infection compared with adults (Loske et al., 2021; Yoshida et al., 2021). In agreement, an early type I IFN response in immune cells was associated with the containment of virus dissemination preventing viral pneumonia (Pekayvaz et al., 2022). However, despite its important endogenous role and several clinical trials demonstrating therapeutic efficacy (Sodeifian et al., 2022), the use of type I IFNs as antiviral treatment has some limitations, mainly due to their ability to augment disease at late time points after infection (Wang et al., 2020).

In contrast, type III IFNs lack such inflammatory effects (Davidson et al., 2016; Galani et al., 2017) and can be used as potent antiviral treatments, even in the absence of fully functional type I IFN immunity (Klinkhammer et al., 2018; Schnepf et al., 2021). A higher IFN-λ to IFN-α/β ratio in critically ill COVID-19 patients correlated with improved disease outcomes, and patients with high expression levels of IFN-λ showed decreased viral loads and accelerated viral clearance (Galani et al., 2021). In line, a small phase II placebo-controlled randomized trial in humans found that treatment of SARS-CoV-2 infected patients with IFN-λ could accelerate viral decline and clearance (Feld et al., 2021), even though a second study failed to demonstrate such significant benefits of IFN-λ treatment (Jagannathan et al., 2021).

The role of type II IFN during COVID-19 on the other hand is much less clear. Although one study reported that the epithelial response to IFN-γ would promote SARS-CoV-2 infection (Heuberger et al., 2021), another study demonstrated significant inhibition of virus replication (Busnadiego et al., 2020). Natural killer (NK) cells from ambulant COVID-19 patients showed increased production of IFN-γ, whereas NK cells from patients with severe COVID-19 produced only low levels of IFN-γ and TNF (Witkowski et al., 2021). This study further demonstrated that an untimely TGF-β response, a cytokine suppressing IFN-γ mediated functions, was limiting the antiviral activity of NK cells. In agreement, others found that NK cells from severe COVID-19 patients were dysfunctional, showing an impairment of antiviral activity that was associated with diminished production of IFN-γ and TNF (Krämer et al., 2021).

Despite the vast amount of clinical data available by now, many questions regarding the disease-causing mechanisms in the elderly remain unresolved. Small animal models are essential to overcome the limitations of human sample heterogeneity and availability. However, most clinical isolates of SARS-CoV-2 cannot infect standard inbred mice, with few exceptions only causing asymptomatic infection (Montagutelli et al., 2021 *Preprint*; Shuai et al., 2021). Although knock-in mice expressing human angiotensin I-converting enzyme 2 (*ACE2*), the receptor for SARS-CoV-2, are permissive to infection with clinical isolates, they do not develop severe or lethal disease (Zhou et al., 2021; Sun et al., 2020; Winkler et al., 2022). Another widely used model that supports severe to lethal disease upon SARS-CoV-2 infection is transgenic mice expressing *ACE2* under the cytokeratin-18 (K18) promotor. While this mouse strain is suitable to test various intervention strategies (Schepens et al., 2021; Wagner et al., 2021), its use to study mechanisms of disease is limited, e.g., by artefactual neuroinvasion of the virus due to abundant and nonphysiological expression of the viral receptor (Winkler et al., 2020). To be able to use existing standard inbred mouse strains, including knockout mice, researchers developed mouse-adapted SARS-CoV-2 strains either by in silico design followed by reverse genetics (Dinnon et al., 2020), by serial passaging (Gu et al., 2020; Rathnasinghe et al., 2021 *Preprint*; Muruato et al., 2021; Gawish et al., 2022; Wong et al., 2022), or by a combination of both (Leist et al., 2020).

In this study, we describe the generation of a highly pathogenic mouse-adapted SARS-CoV-2 strain (designated SARS-CoV-2 MA20 [MA20]) that dose-dependently causes mild, severe, or even lethal disease progression in 8–20-wk-old (designated adult) C57BL/6 WT mice. In 36–60-wk-old (designated aged) C57BL/6 mice, disease severity was strongly enhanced and associated with (i) lack of an early and well-coordinated innate and adaptive immune response, (ii) markedly increased viral load, and (iii) late inflammatory response. Direct comparison of adult and aged knockout mice showed that defective type I and type II IFN signaling phenocopies enhanced disease progression in aged mice, providing a mechanistic explanation for the age-related increase in disease susceptibility during SARS-CoV-2 infection.

Using adult mice lacking a functional IFN-α/β receptor (*Ifnar1*$^{-/-}$) to mimic impaired type I IFN immunity (Bastard et al., 2021; Bastard et al., 2020; Zhang et al., 2020), we show that prophylactic or therapeutic administration of IFN-λ efficiently protected such mice when lethally infected. Nevertheless, IFN-λ treatment alone had limited protective effects in highly vulnerable aged *Ifnar1*$^{-/-}$ mice. However, administration of IFN-γ in aged WT mice reversed the age-dependent enhanced disease phenotype, and a combinatorial treatment with IFN-λ and IFN-γ even protected highly vulnerable aged *Ifnar1*$^{-/-}$ mice against lethal diseases.

By generating and employing a mouse model for severe COVID-19, we identified the age-dependent impairment of type I and type II IFN responses as a critical pathomechanism that drives the virulence of SARS-CoV-2 in aged hosts. This novel insight was successfully translated into an immunomodulatory treatment strategy that prevented SARS-CoV-2–induced lethality in a highly susceptible disease model that mimics impaired type I IFN immunity and advanced age.

Results

Type I and type III IFNs synergize to limit SARS-CoV-2 replication and protect aged mice against symptomatic disease

To dissect the individual and combinatorial roles of type I and type III IFNs in limiting SARS-CoV-2 replication, we compared the replication kinetics of a mouse-adapted but largely

nonvirulent SARS-CoV-2 strain (SARS-CoV-2 MA [Dinnon et al., 2020]) in IFN receptor-deficient and C57BL/6 WT mice. Three days postinfection (d p.i.), we found about 10-fold increased viral loads in lungs and upper airways of mice lacking functional type I (*Ifnar1*$^{-/-}$) or type III IFN receptors (*Ifnlr1*$^{-/-}$; Fig. 1 A and Fig. S1 A). By day 5 p.i., most WT mice had cleared the virus, whereas *Ifnar1*$^{-/-}$, especially *Ifnlr1*$^{-/-}$, mice continued to have high viral titers in their lungs (Fig. 1 A). Conversely, prophylactic or therapeutic administration of either IFN-$\alpha_{B/D}$ (Klinkhammer et al., 2018) to *Ifnlr1*$^{-/-}$ or IFN-λ1/3 (Yu et al., 2016) to *Ifnar1*$^{-/-}$ mice reduced lung viral loads on day 3 p.i. by several orders of magnitude (Fig. 1 B and Fig. S1 B). Combinatorial loss of type I and type III IFN signaling in *Ifnar1*$^{-/-}$*Ifnlr1*$^{-/-}$ mice led to excessive replication and prolonged persistence of the virus in upper airways and lungs (Fig. 1 A and Fig. S1 A). Immunohistochemical analyses confirmed increased virus replication and prolonged virus persistence in *Ifnar1*$^{-/-}$*Ifnlr1*$^{-/-}$ compared with WT mice (Fig. S1, C and D), mainly affecting the bronchial epithelium and only scarcely alveolar epithelial cells. Lung tissue damage (Fig. S1 E) and necrotizing bronchitis (Fig. S1 F) followed the pattern of increased and prolonged virus replication in *Ifnar1*$^{-/-}$*Ifnlr1*$^{-/-}$ mice. However, despite increased and prolonged viral replication and tissue damage, we did not observe weight loss or other signs of disease in adult mice lacking type I and/or type III IFN responses (Fig. 1 C). In contrast, using aged animals in an identical infection setting, we observed significantly increased weight loss in *Ifnar1*$^{-/-}$, *Ifnlr1*$^{-/-}$, and *Ifnar1*$^{-/-}$*Ifnlr1*$^{-/-}$ mice compared with age-matched WT controls (Fig. 1 D), sporadically even leading to lethal disease progression in case of *Ifnar1*$^{-/-}$*Ifnlr1*$^{-/-}$ mice (Fig. S1 G). Of note, we did not observe increased weight loss in aged WT mice compared with adult controls (Fig. 1, C and D), indicating that a combination of advanced age and impaired type I/III IFN immunity is required to result in symptomatic disease during infection with the SARS-CoV-2 MA strain.

Taken together, these data demonstrated that type I and type III IFNs synergize to limit excessive SARS-CoV-2 replication, expedite virus clearance, and protect against symptomatic disease in aged mice.

Advanced age correlates with increased viral loads and diminished immune responses

To gain more insight into the age-dependent disease phenotype of SARS-CoV-2 MA, we compared tissue sections from upper airway and lung samples of infected adult and aged *Ifnar1*$^{-/-}$ mice. 3 d p.i., we detected increased antigen load in upper airways and lungs as well as enhanced bronchial necrosis in aged *Ifnar1*$^{-/-}$ mice (Fig. S1, H–J). Comparing viral growth kinetics in adult and aged WT, *Ifnar1*$^{-/-}$, *Ifnlr1*$^{-/-}$, and *Ifnar1*$^{-/-}$*Ifnlr1*$^{-/-}$ mice, we confirmed the age-dependent increase in virus replication at 3 d p.i., irrespective of genotype (Fig. 1, E and F and Fig. S1 K). Similar to adult mice (Fig. 1 A), combinatorial loss of type I and type III IFN signaling in aged *Ifnar1*$^{-/-}$*Ifnlr1*$^{-/-}$ mice (Fig. 1 F) led to significantly increased viral loads compared with WT or single knockout mice (Fig. 1 E), demonstrating that aged WT mice rely on synergistic effects of type I and III IFNs to control virus replication.

To identify impaired antiviral or enhanced proviral pathways facilitating virus replication in aged mice that are independent of type I/III IFN signaling, we performed transcriptome analyses using lung samples of infected or mock-treated adult and aged *Ifnar1*$^{-/-}$ mice. Gene Set Enrichment Analyses (GSEA) comparing mock-treated (Fig. 1 G) or infected (Fig. 1 H) adult and aged *Ifnar1*$^{-/-}$ mice identified an age-related increase in pathways involved in the function of ciliated cells, possibly suggesting age-dependent differences in the cellular composition of the lung. Although no pathways were significantly enriched in uninfected adults compared with aged mice, lung tissue samples from infected adult mice showed significant enrichment in pathways involved in the production and response to IFN-γ, NK cell–mediated immunity, immune cell activation, and adaptive immune responses (Fig. 1 H), which indicated a versatile and robust immune response in adult animals. The disruption of a timely and well-coordinated innate and adaptive immune response in aged mice upon SARS-CoV-2 infection could explain impaired virus control, ultimately leading to enhanced disease progression.

These data demonstrate that the age-dependent increase in virus replication is independent of type I and type III IFN signaling but associated with an age-related impaired immune response affecting IFN-γ production, NK cell–mediated immunity, and immune cell activation in general.

Rapid host adaptation by serial passaging in type I/III IFN receptor-deficient C57BL/6 mice

To study the age-related pathophysiology of SARS-CoV-2–induced disease in more detail and to test possible intervention strategies, we generated a mouse model resembling severe COVID-19 by serially passaging the SARS-CoV-2 MA strain in-vivo. In total, we performed four independent passaging series, two in C57BL/6 WT (WT A and B) and two in *Ifnar1*$^{-/-}$*Ifnlr1*$^{-/-}$ mice (DKO A and B; Fig. 2 A). From passage 10 onwards, *Ifnar1*$^{-/-}$*Ifnlr1*$^{-/-}$ but not WT mice were losing increasing amounts of their initial body weight (Fig. 2 B). Although viral titers in lungs remained relatively stable until passage 20, viral loads in the upper airways increased from passage 14 onwards for series WT B, DKO A, and DKO B (Fig. S2, A and B). To identify which passaging series contained pathogenic variants, we infected groups of C57BL/6 WT mice with passage 20 (P20) lung homogenates containing 10^4 PFU of virus and followed the course of disease and survival rates (Fig. 2 C). Virus variants derived from passaging series WT A and B did not induce severe signs of disease, whereas P20 homogenates from passaging series DKO A and DKO B induced severe weight loss and even 40% lethality in adult C57BL/6 WT mice in case of DKO A P20. Using plaque-purified (PP) virus stocks derived from DKO A and DKO B P20 lung homogenates, we confirmed the successful generation of a pathogenic mouse-adapted SARS-CoV-2 variant that emerged in passaging series DKO A (Fig. S2 C). Virus genome sequencing revealed that this variant, named MA20, acquired eight additional amino acid changes compared with the parental SARS-CoV-2 MA strain (Fig. 2 D), three in S (T250A, K417N, and Q493H), one in M (T7I), and four in ORF1ab (A1997V, T3058I, D4165Y, and T4174A) that translate into A1179V in nsp3, T295I in

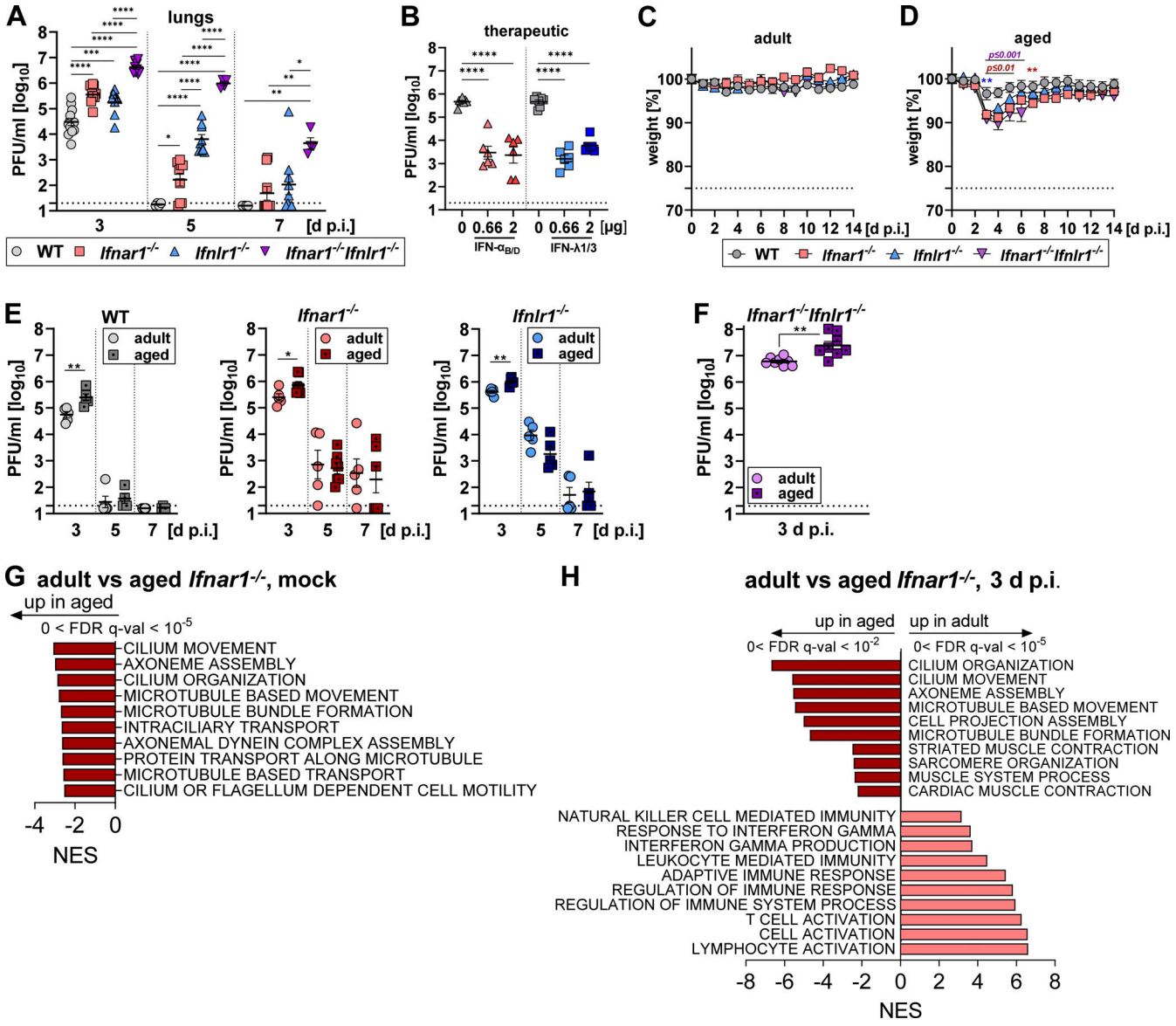

Figure 1. **Impaired type I/III IFN signaling and advanced age in combination lead to enhanced disease during SARS-CoV-2 MA infection. (A)** Groups of adult (8–18-wk-old) mice of the indicated genotypes were infected with 10^5 PFU SARS-CoV-2 MA. Lungs were harvested at the indicated time points and viral loads were determined by plaque assay on Vero E6 cells. Data pooled from five independent experiments. Symbols represent individual mice (n = 4–13 per group) and bars indicate mean ± SEM. Dashed line indicates detection limit. *P ≤ 0.05, **P ≤ 0.01, ***P ≤ 0.001, ****P ≤ 0.0001, one-way ANOVA with Tukey's multiple comparisons test. **(B)** Groups of 16–24-wk-old *Ifnlr1*$^{-/-}$ (triangles) and *Ifnar1*$^{-/-}$ mice (squares) were treated intranasally with the indicated doses of IFN-$\alpha_{B/D}$ or IFN-λ1/3, respectively, or mock-treated, 1 d after infection with 10^5 PFU SARS-CoV-2 MA. Lung viral loads on day 3 p.i. were determined by plaque assay on Vero E6 cells. Data from a single experiment are shown. Symbols represent individual mice (n = 6–7 per group) and bars indicate mean ± SEM. Dashed line indicates detection limit. ****P ≤ 0.0001, one-way ANOVA with Tukey's multiple comparisons test. **(C and D)** Groups of adult (10–15-wk-old; n = 7–8; C) or aged (36–60-wk-old; n = 10–19; D) mice of the indicated genotypes were infected with 10^5 PFU SARS-CoV-2 MA. Signs of disease and weight loss were monitored for 14 d. Data from a single experiment are shown in C and pooled data from two independent experiments are shown in D. Symbols represent mean ± SEM. Dashed line indicates experimental endpoint due to animal welfare. Two-way ANOVA with Tukey's multiple comparisons test comparing WT with *Ifnar1*$^{-/-}$ (red), *Ifnlr1*$^{-/-}$ (blue), and *Ifnar1*$^{-/-}$*Ifnlr1*$^{-/-}$ (purple), **P ≤ 0.01. **(E)** Groups of adult (8–12-wk-old) or aged (40–60-wk-old) mice (n = 4–7) of the indicated genotypes were infected with 10^5 PFU SARS-CoV-2 MA. Lungs were harvested at the indicated time points and viral loads determined by plaque assay on Vero E6 cells. Data pooled from four independent experiments are shown. Symbols represent individual mice and bars indicate mean ± SEM. Dashed line indicates detection limit. *P ≤ 0.05, **P ≤ 0.01, unpaired t test. **(F)** Groups of adult (9-wk-old) or aged (60-wk-old) *Ifnar1*$^{-/-}$*Ifnlr1*$^{-/-}$ mice (n = 8) were infected with 10^5 PFU SARS-CoV-2 MA. Lungs were harvested on day 3 p.i. and viral loads determined by plaque assay on Vero E6 cells. Data from a single experiment are shown. Symbols represent individual mice and bars indicate mean ± SEM. **P ≤ 0.01, unpaired t test. **(G and H)** Groups of adult (12-wk-old) or aged (44-wk-old) *Ifnar1*$^{-/-}$ mice (n = 5) were mock-infected (G) or infected with 10^5 PFU SARS-CoV-2 MA (H). Lungs were harvested on day 3 p.i. and processed for RNA-sequencing. GSEA of ranked genes indicating strong enrichment for immune cell activation pathways in infected adult compared with aged mice. Negative and positive normalized enrichment scores (NES) indicate enrichment in aged and adult *Ifnar1*$^{-/-}$ mice, respectively. FDR <10^{-2} for all pathways is shown.

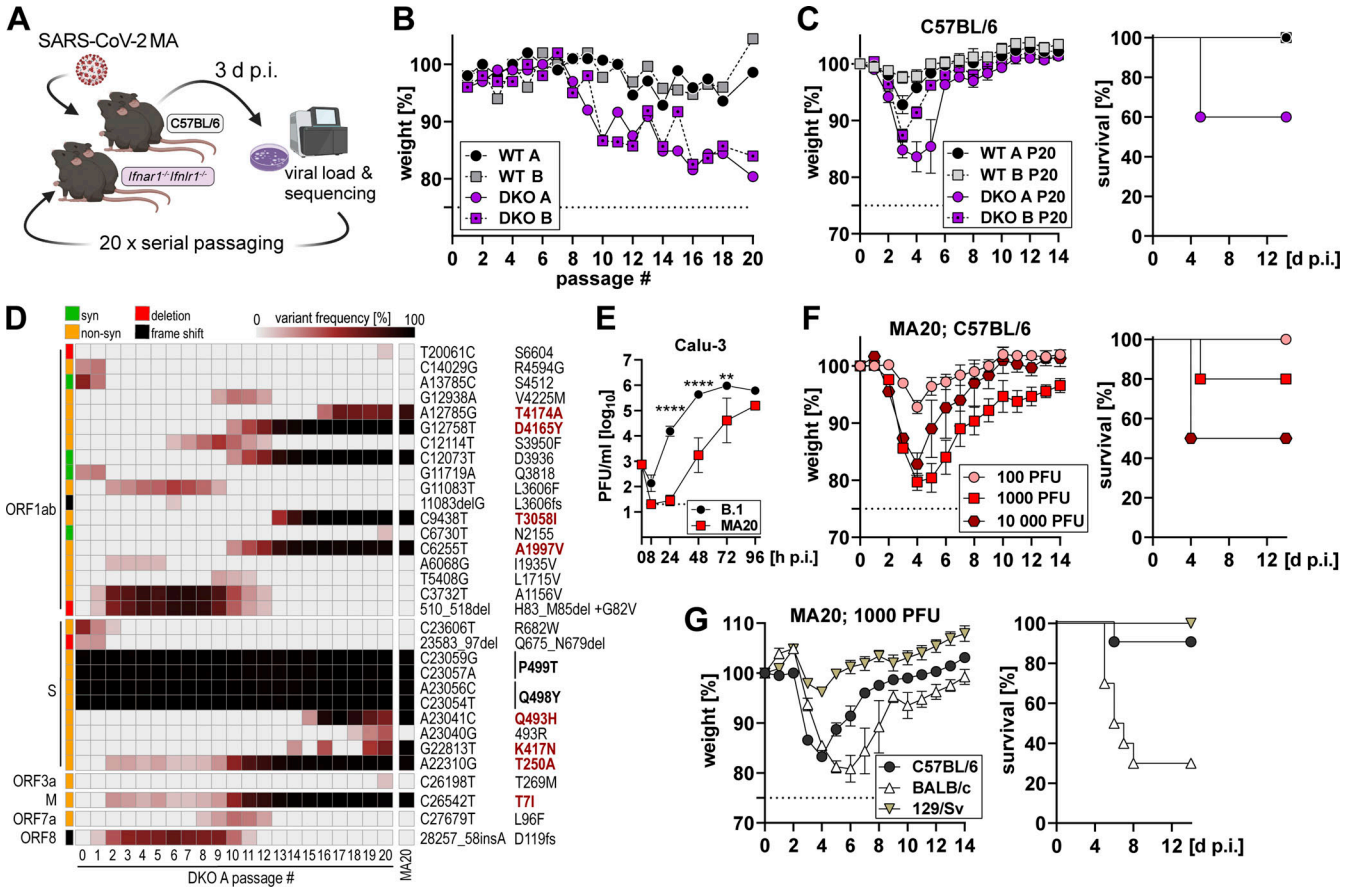

Figure 2. **Serial passaging of SARS-CoV-2 MA in *Ifnar1*$^{-/-}$*Ifnlr1*$^{-/-}$ C57BL/6 mice yielded a highly virulent virus variant. (A)** Schematic overview of serial passaging of SARS-CoV-2 MA in C57BL/6 (WT A and B) and B6-*Ifnar1*$^{-/-}$*Ifnlr1*$^{-/-}$ mice (DKO A and B). Mice were initially infected with 10^5 PFU SARS-CoV-2 MA. Serial passaging was performed by infecting mice with lung homogenates containing 10^3–10^5 PFU. Lungs were harvested on day 3 p.i. **(B)** Weight loss of C57BL/6 (WT A and B) and B6-*Ifnar1*$^{-/-}$*Ifnlr1*$^{-/-}$ mice (DKO A and B) per passage on day 3 p.i. Symbols represent individual mice. Dashed line indicates experimental endpoint due to animal welfare. **(C)** Weight loss (left panel) and survival (right panel) of adult C57BL/6 WT mice (8–10-wk-old; *n* = 5 per group) infected with diluted P20 lung homogenates derived from passaging series WT A, WT B, DKO A, and DKO B containing 10^4 PFU. Data from a single experiment are shown. Symbols represent mean ± SEM. Dashed line indicates experimental endpoint due to animal welfare. **(D)** Variant frequency plot from next-generation sequencing results for passaging series DKO A and the PP MA20 virus stock. Variant frequencies are shown in comparison to Wuhan-Hu-1 (NC_045512.2). Amino acid changes present in SARS-CoV-2 MA20 are indicated in bold, changes in comparison to SARS-CoV-2 MA are highlighted in red. Syn = synonymous; non-syn = non-synonymous. **(E)** Comparative growth curves of SARS-CoV-2 strains B.1 and MA20 on Calu-3 cells infected with an MOI of 0.001. Virus replication was quantified by plaque assay on Vero E6 cells. Data from a single experiment performed in duplicates are shown. Dashed line indicates detection limit. **P ≤ 0.01, ****P ≤ 0.0001, two-way ANOVA with Tukey's multiple comparisons test. **(F)** Weight loss (left panel) and survival (right panel) of adult C57BL/6 mice (10–14-wk-old; *n* = 5–10 per group) infected with the indicated dose of MA20. Pooled data from three independent experiments are shown. Symbols represent mean ± SEM. Dashed line indicates experimental endpoint due to animal welfare. **(G)** Weight loss (left panel) and survival (right panel) of adult C57BL/6, 129/Sv, or BALB/c mice (10-wk-old; *n* = 10 per group) infected with 10^3 PFU MA20. Data from a single experiment are shown. Symbols represent mean ± SEM. Dashed line indicates experimental endpoint due to animal welfare.

nsp4, and D25Y and T34A in nsp9. Of note, identical or similar amino acid substitutions such as the Q493H and K417N in the spike protein are also present in other mouse-adapted SARS-CoV-2 variants (Leist et al., 2020; Rathnasinghe et al., 2021 *Preprint*; Wong et al., 2022) or circulating variants of concern including B.1.1.529 (Omicron; Fig. S2, D and E). Productive infection of human A549 cells by MA20 remained ACE2 dependent (Fig. S2 F). Despite its increased pathogenicity in mice, SARS-CoV-2 MA20 replication was strongly attenuated in human Calu-3 and simian Vero E6 cells (Fig. 2 E and Fig. S2 G). In addition, MA20 is even better neutralized by sera from vaccinated humans compared with the B.1.617.2 (Delta) variant (Fig. S2 H). Using doses of MA20 ranging from 10^2 to 10^4 PFU, we could model mild, moderate, or even lethal SARS-CoV-2–induced disease progression in adult C57BL/6 WT mice (Fig. 2 F). By infecting age- and sex-matched C57BL/6, BALB/c, and 129/sv mice with 10^3 PFU of MA20, we found that BALB/c mice were highly susceptible with a survival rate of only 30%, 129/sv mice were mostly resistant to disease, and C57BL/6 showed intermediate susceptibility with substantial weight loss but a survival rate of 90% (Fig. 2 G).

Next, we performed virus growth kinetics in groups of C57BL/6 WT mice using 10^3 PFU of MA20 and monitored virus shedding via the nostrils (Fig. 3 A) and virus replication in upper airways (Fig. 3 B) and lungs (Fig. 3 C). Infection-induced gene

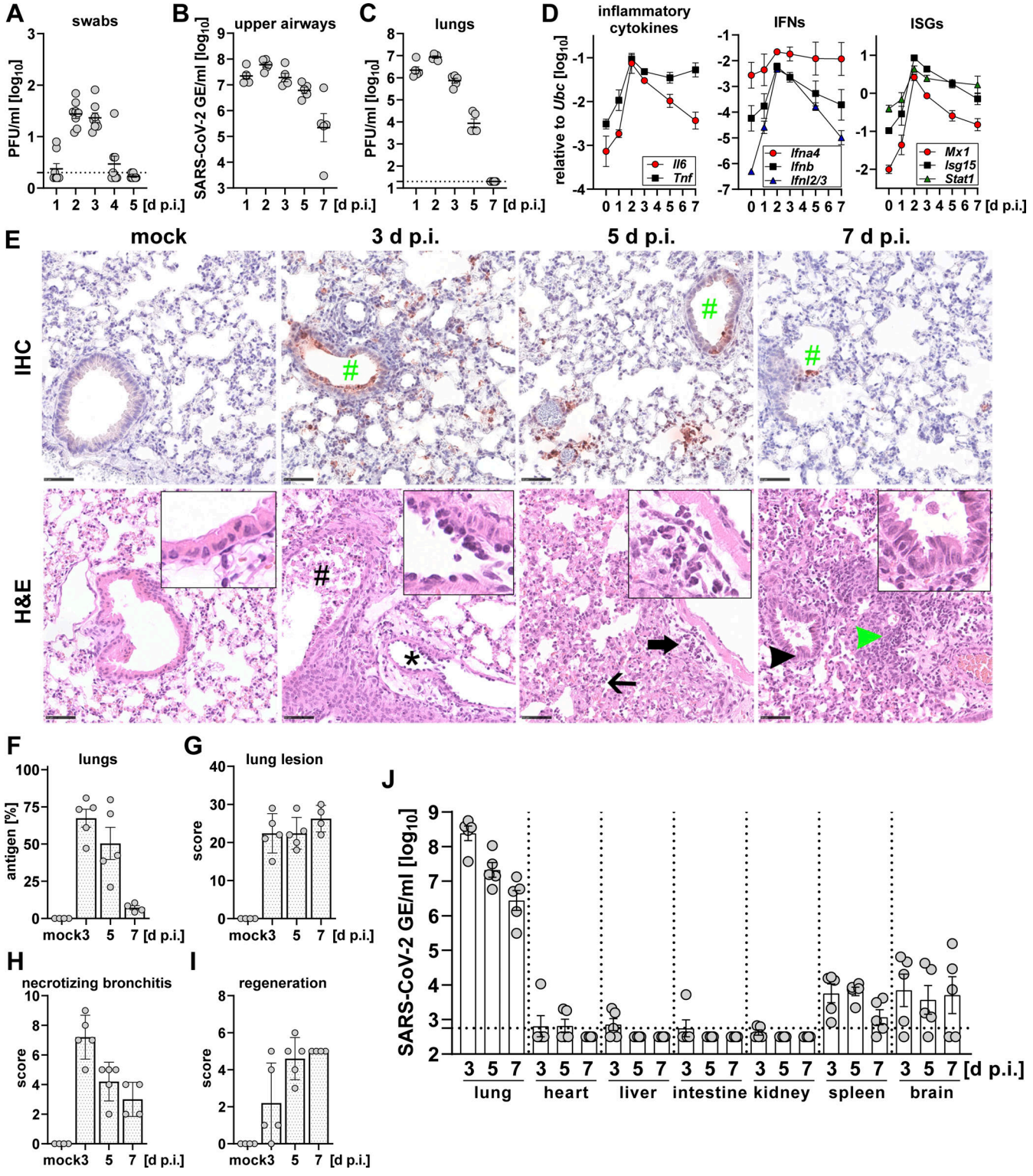

Figure 3. **MA20 efficiently replicates in upper airways and lungs of adult C57BL/6 mice, inducing innate immune responses and tissue damage. (A–J)** Adult C57BL/6 mice (8–17-wk-old; *n* = 4–8 per group) were mock-treated or infected with 10^3 PFU MA20. Samples were collected at the indicated time points. **(A)** Nasal swabs were taken at the indicated time points and viral loads were determined by plaque assay on Vero E6 cells. Symbols represent individual mice and bars indicate mean ± SEM. Dashed line indicates detection limit. **(B)** Viral replication in upper airways was quantified as SARS-CoV-2 genome equivalents per ml by measuring expression levels of the viral gene *E* by RT-qPCR at the indicated time points. Symbols represent individual mice and bars indicate mean ± SEM. **(C)** Viral load in lungs was determined by plaque assay on Vero E6 cells at the indicated time points. Symbols represent individual mice and bars indicate mean ± SEM. Dashed line indicates detection limit. **(D)** Gene expression levels of *Il6*, *Tnf*, *Ifna4*, *Ifnb*, *Ifnl2/3*, *Mx1*, *Isg15*, and *Stat1* in lungs were determined relative to *Ubc* by RT-qPCR. Symbols represent mean ± SD. **(E–I)** Mice were prepared for histological analyses by cardiac perfusion at the indicated time points. **(E)** Representative pictures for IHC and histopathology are shown. Bar indicates 50 µm. Green hashtag: viral antigen in bronchi (3 and 5 d p.i.) and terminal

bronchioles (7 d p.i.); black hashtag: necrotizing bronchitis with intraluminal cellular debris; asterisk and inlay above: blood vessel with leukocyte rolling and activation of endothelial cells; bold arrow and inlay above: perivascular infiltrates, mainly neutrophils; narrow arrow: alveolar infiltrates, mainly neutrophils; black arrowhead and inlay above: bronchial epithelial hypertrophy/hyperplasia, see mock-treated mice (inlay) for comparison; green arrowhead: perivascular infiltrates extending into adjacent interstitium, mainly lymphocytes, fewer macrophages and neutrophils. Antigen (F), histopathologic lesion scores for lungs (G), necrotizing bronchitis (H), and regeneration scores (I) were quantified as described in Materials and methods section. **(J)** Viral RNA levels in lung, heart, liver, intestine, kidney, spleen, and brain were quantified as SARS-CoV-2 genome equivalents per ml by measuring expression levels of the viral gene *E* by RT-qPCR at the indicated time points. Symbols represent individual mice and bars indicate mean ± SEM. Dashed line indicates detection limit.

expression levels of inflammatory cytokines such as *Il6* and *Tnf*, type I (*Ifna4* and *Ifnb*), and type III IFNs (*Ifnl2/3*) as well as ISGs such as *Mx1*, *Isg15*, and *Stat1* peaked simultaneously with peak viral loads on day 2 p.i. in lungs and upper airways (Fig. 3 D and Fig. S2 I). By day 7 p.i., no infectious virus could be detected anymore, which was in line with histopathological findings that viral antigens were mostly cleared by day 7 (Fig. 3, E and F). Despite rapidly decreasing lung viral loads (Fig. 3 C), lung tissue damage remained at high scores until day 7 (Fig. 3 G). Compared with the less virulent SARS-CoV-2 MA strain, the highly pathogenic MA20 variant caused a more widespread infection of the lung tissue as indicated by increased antigen-positive areas (Fig. S1 I and Fig. 3 F; about 10% mean antigen detection in SARS-CoV-2 MA infected adult *Ifnar1*$^{-/-}$ 3 d p.i., compared with about 67% mean antigen detection in MA20 infected adult WT mice 3 d p.i.). Besides the bronchial epithelium (Fig. 3 E, green hashtag), mainly alveolar epithelial cells were found to be virus-positive, in particular type 2 pneumocytes. In line with acute viral pneumonia, lung lesions were characterized by necrotizing bronchitis (Fig. 3 E, black hashtag), most severely affecting mice on day 3 p.i. (Fig. 3 H). The extent and severity decreased over time, but bronchial lesions were still detectable until day 7 p.i. in all animals analyzed. Perivascular infiltrates comprised mainly of neutrophils (Fig. 3 E, bold arrow and inlay) and few lymphocytes. The latter partly dominated at later time points (Fig. 3 E, green arrowhead). Focal to multifocal necrosis of the alveolar epithelium was associated with minimal to moderate alveolar infiltrates (Fig. 3 E, narrow arrow). Tissue regeneration in some animals could be detected as early as 3 d p.i. and consistently increased until day 7 p.i. (Fig. 3 I), as indicated by bronchial epithelial hypertrophy and hyperplasia (Fig. 3 E, black arrowhead and inlay) as well as type 2 pneumocyte hyperplasia. In single cases, we found atypical multinucleated (syncytial) cells, increased mucus production, and endotheliitis. Numerous examples of leukocyte rolling (Fig. 3 E, 3 d p.i. asterisk and inlay) were found in blood vessels of infected animals, indicating endothelial and/or immune cell activation. Interstitial infiltrates were rarely detected. Neither vasculitis nor diffuse alveolar damage was diagnosed. Examining other organs by quantitative RT-PCR (RT-qPCR) for the presence of viral RNA, we found low levels in brain and spleen samples and infrequently positive heart, liver, intestine, and kidney samples, indicating that replication of SARS-CoV-2 MA20 is mainly restricted to the upper and lower respiratory tract in adult mice (Fig. 3 J).

These data show that serial passaging in *Ifnar1*$^{-/-}$*Ifnlr1*$^{-/-}$ mice facilitated rapid host adaption, which resulted in the highly virulent MA20 variant that can be used to model mild, severe, or even lethal COVID-19 in standard inbred mice.

Enhanced disease progression in aged mice correlates with a diminished immune response leading to insufficient control of virus replication

Disease severity and risk of death due to COVID-19 show a log-linear correlation with advanced age in humans (O'Driscoll et al., 2021). Correspondingly, aged mice showed a massively enhanced disease phenotype and increased lethality upon infection with MA20 compared with adult counterparts (Fig. S3 A). To mechanistically address the age-dependent enhanced disease progression, we chose infection conditions that cause a comparable weight loss from which adult but not aged mice could recover (Fig. 4 A), and we measured virus replication kinetics, determined systemic dissemination of viral material, assessed lung tissue damage, and compared kinetics of the age-dependent immune response profiles in infected lungs.

Between day 3 and 5 p.i., virus replication in upper airways (Fig. 4 B) and lungs (Fig. 4 C) of aged mice was found to be increased by one to two orders of magnitude compared with genetically identical adult controls, demonstrating an age-dependent impairment of virus control. For both, adult and aged mice, viral antigen was found abundantly in the bronchial and alveolar epithelium (Fig. 4 D, green hashtags for bronchial, arrowheads for alveolar cells), in particular in type 2 pneumocytes. However, viral antigen was significantly more widespread in infected lung sections of aged mice compared with adult counterparts (Fig. 4 D, restriction of viral antigen mainly around bronchi illustrated by arrowheads for adult mice and almost diffuse labeling in aged animals, and Fig. 4 E), indicating that large areas of the aged lungs were compromised by viral infection. Intriguingly, overall lung lesion scores were comparable between both age groups under these infection conditions at the given time points evaluated (Fig. 4 D, 4 d p.i. black hashtag for intraluminal cellular debris due to necrotizing bronchitis and bold arrows for peribronchial and perivascular infiltrates, and Fig. 4 F), even though signs of disease were much more pronounced in MA20-infected aged mice. This may suggest that extensive and widespread viral infection of alveolar epithelial cells leads to functional impairment of the lung even before major tissue damage becomes apparent. Similarly, independent of age, all infected mice showed vascular leukocyte rolling and activation of endothelial cells (Fig. 4 D, exemplarily shown for 3 d p.i., inlay). Acute necrotizing bronchitis showed a slight tendency to be increased in aged mice on 5 d p.i. (Fig. 4 G), and tissue regeneration indicated by bronchial epithelial hypertrophy and hyperplasia as well as type 2 pneumocyte hyperplasia appeared to be less prominent in aged animals (Fig. 4 D, 5 d p.i., narrow arrow and inlay, Fig. 4 H). As described above, only single animals showed increased mucus production, endotheliitis, and/or interstitial infiltrates. Neither syncytial cells nor

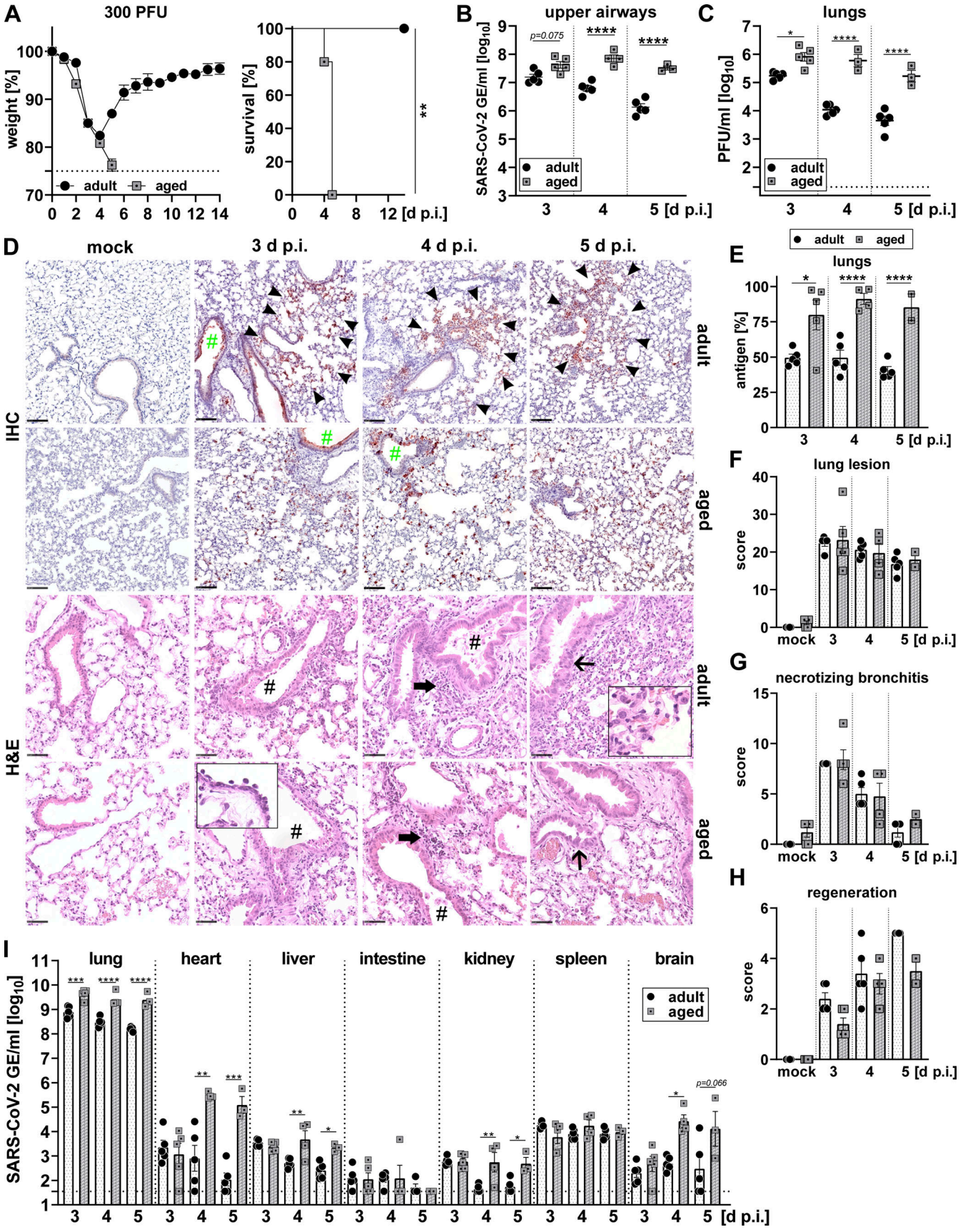

Figure 4. **Enhanced susceptibility of aged mice to SARS-CoV-2–induced disease is associated with increased viral loads. (A–I)** Groups of adult or aged (10-wk- or 40-wk-old) C57BL/6 mice were infected with 300 PFU MA20. Subgroups of mice were sacrificed at the indicated time points to quantify virus

replication and to evaluate virus-induced tissue damage. **(A)** Weight loss (left panel) and survival (right panel) were monitored for 14 d p.i. Data from a single experiment are shown. Symbols represent mean ± SEM. Dashed line indicates experimental endpoint due to animal welfare. Survival: **P ≤ 0.01, Log-rank (Mantel-Cox) test, *n* = 5 per group. **(B)** Viral replication in upper airways was quantified as SARS-CoV-2 genome equivalents per ml by measuring expression levels of the viral gene *E* by RT-qPCR at the indicated time points. Data from a single experiment are shown. Symbols represent individual mice and bars indicate mean ± SEM. ****P ≤ 0.0001, one-way ANOVA with Tukey's multiple comparisons test, *n* = 3–5 per group. **(C)** Viral load in lungs was determined by plaque assay on Vero E6 cells at the indicated time points. Data from a single experiment are shown. Symbols represent individual mice and bars indicate mean ± SEM. Dashed line indicates detection limit. *P ≤ 0.05, ****P ≤ 0.0001, one-way ANOVA with Tukey's multiple comparisons test, *n* = 3–5 per group. **(D–H)** Groups of mice (*n* = 2–5) were prepared for histological analyses by cardiac perfusion at the indicated time points. **(D)** Representative pictures for IHC and histopathology are shown. Bar indicates 100 µm for IHC or 50 µm for H&E. Green hashtag: viral antigen in bronchial cells; arrowheads: viral antigen in alveolar cell; note the restriction of viral antigen in adult mice mainly around bronchi but almost diffuse (no arrowheads) labeling in aged animals; black hashtag: necrotizing bronchitis; bold arrow: perivascular on peribronchial infiltrates; narrow arrow: bronchial epithelial hyperplasia/hypertrophy, more pronounced and with inlay showing type II pneumocyte hyperplasia in adult mice 7 d p.i.; inlay for H&E 3 d p.i. showing vascular leukocyte rolling with endothelial activation. Antigen (E), histopathologic lesion scores for lungs (F), necrotizing bronchitis (G), and regeneration scores (H) were quantified as described in Materials and methods section. **(D–H)** Data from a single experiment are shown, *n* = 2–5 per group. Symbols represent individual mice and bars indicate mean ± SEM. **(E)** *P ≤ 0.05, ****P ≤ 0.0001, one-way ANOVA with Tukey's multiple comparisons test. **(I)** Viral RNA in lungs, heart, liver, intestine, kidney, spleen, and brain was quantified as SARS-CoV-2 genome equivalents per ml by measuring expression levels of the viral gene *E* by RT-qPCR at the indicated time points. Symbols represent individual mice and bars indicate mean ± SEM. Dashed line indicates detection limit. *P ≤ 0.05, **P ≤ 0.01, ***P ≤ 0.001, one-way ANOVA with Tukey's multiple comparisons test, *n* = 3–5 per group.

vasculitis or diffuse alveolar damage were found. Investigating the potential systemic dissemination of virus material, we found viral RNA levels to be significantly increased in heart, liver, kidney, and brain samples of aged mice compared with adult controls on days 4 and 5 p.i. (Fig. 4 I). However, using immunohistochemistry (IHC) and RNA in situ hybridization (ISH) methods, no viral antigen or RNA could be detected in heart and brain samples (data not shown). Furthermore, histology of brain and heart revealed no abnormalities and neither IHC for T-cells (CD3) nor microglia/macrophages (Iba-1) identified inflammatory infiltrates or microglial reaction (data not shown). In the absence of evidence of productive infection of cells in heart or brain tissue, as well as the absence of inflammatory infiltrates, we concluded that virus replication mainly was restricted to the respiratory tract in both, adult and aged mice.

Next, we compared the kinetics of transcriptional responses in MA20-infected lungs of adult and aged mice. Principal component analysis of the lung transcriptome showed that uninfected adult and aged mice closely clustered together, indicating that basal gene expression profiles in uninfected lungs of adult and aged mice were rather similar (Fig. 5 A). In contrast, transcriptional profiles of infected lung samples clearly diverged dependent on the respective age group for all time points analyzed, demonstrating a drastically different transcriptional response to SARS-CoV-2 infection between the two age groups (Fig. 5 A). GSEA comparing each time point between adult and aged mice revealed that adult animals mounted a rapid and versatile innate and adaptive immune response. In contrast, the immune response of aged animals was delayed, reduced in pathways leading to adaptive immunity, and was mainly proinflammatory. From 3 d p.i. onwards, innate immune pathways involving IFN-γ signaling and NK cell activity but also adaptive cellular and humoral immune responses were significantly enriched in adult animals compared with aged controls (Fig. 5 B). By contrast, in aged animals, primarily proinflammatory pathways driven by IL-6, IL-1, and type I IFN were found to be significantly enriched upon day 4 p.i. compared with samples derived from adult animals. Pairwise comparison of infected to mock lung samples from adult or aged animals at different time points after infection using Ingenuity Pathway Analysis (IPA) confirmed that adult animals were mounting a rapid and well-orchestrated innate and adaptive immune response, characterized by the initiation of PRR signaling, NK cell activation, and the production and response to Th1/Th2 cytokines (Fig. 5 C). In contrast, aged animals showed a reduced, delayed, and more proinflammatory response. In addition to IL-6– and IL-1–driven pathways, IPA also identified active processes of pulmonary fibrosis and hypoxia-induced gene regulation in infected lung tissue of aged mice (Fig. 5 C). Intriguingly, aged animals also showed an early and strong IL-10 response (Trinchieri, 2007; Couper et al., 2008), which further emphasizes the imbalanced early immune response in aged animals and might explain the lack of a potent immune response initiated by IFN-γ and other immune activating cytokines as observed in adult mice.

Taken together, these data demonstrate that the age-dependent increase in disease susceptibility upon SARS-CoV-2 infection correlates with impaired virus control due to imbalanced and insufficient innate and adaptive immune responses.

Combinatorial defects in type I and type II IFN signaling phenocopies age-dependent disease susceptibility

Using 300 PFU of the highly virulent MA20 strain, we determined the disease susceptibility of adult mice lacking functional type I and/or type III IFN systems. Single knockout mice deficient in type I or type III IFN–mediated responses had comparable survival rates as WT mice but suffered from increased and prolonged weight loss (Fig. 6 A). In contrast, mice lacking both systems rapidly lost weight, and most animals reached experimental endpoints and had to be euthanized (Fig. 6 A). As the disease course of adult *Ifnar1*$^{-/-}$*Ifnlr1*$^{-/-}$ mice closely resembled the one in aged WT mice (Fig. 4 A), we performed low-dose infection experiments with MA20 in adult and aged mice of matching genotypes to assess whether the age-dependent increase in disease susceptibility was caused by an impaired IFN response. Using 30 PFU of MA20, we detected a significantly enhanced disease progression in aged WT, and in addition, significantly increased lethality in aged *Ifnar1*$^{-/-}$, *Ifnlr1*$^{-/-}$, and

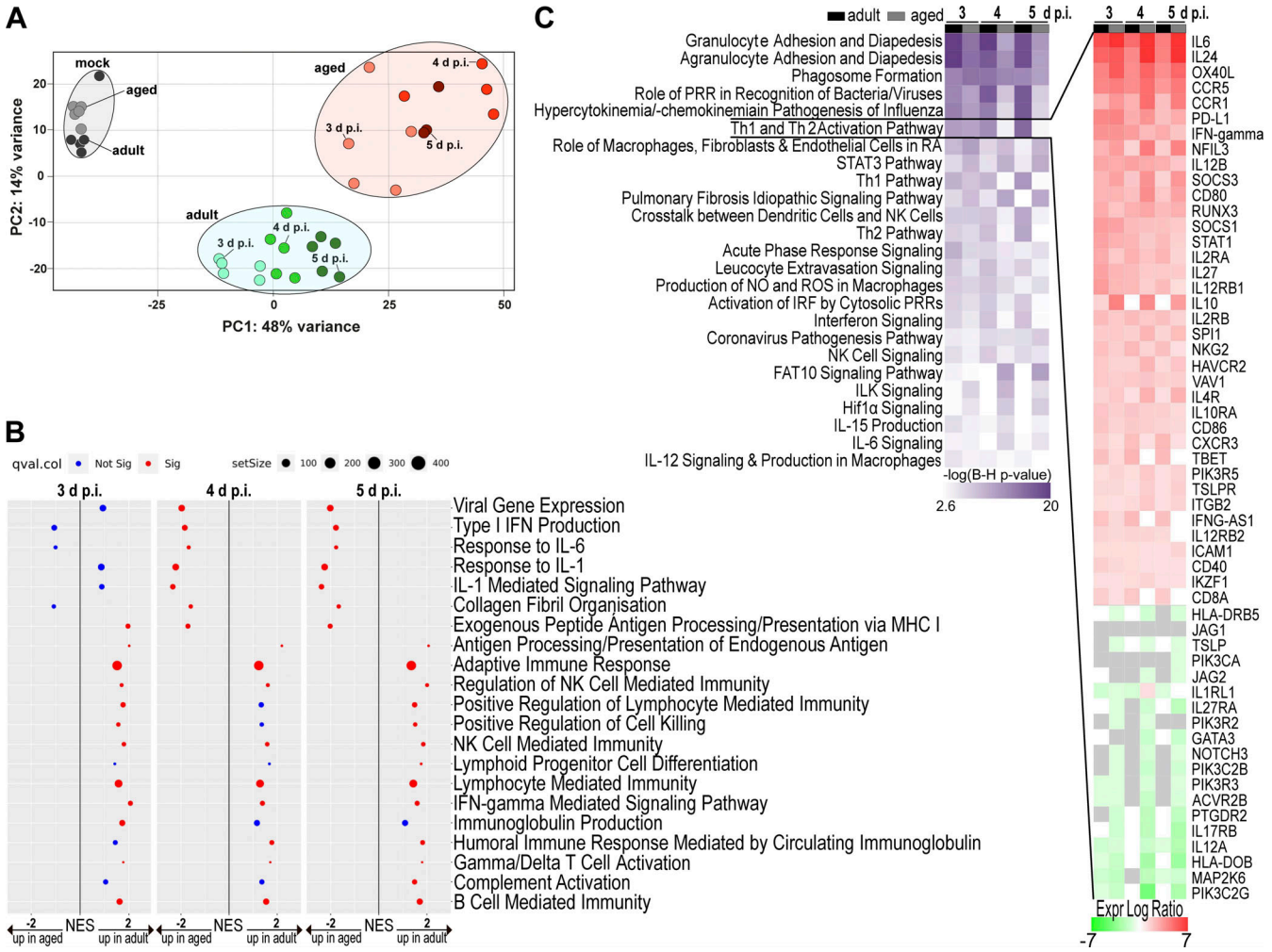

Figure 5. **Immune response in SARS-CoV-2 infected aged mice is delayed, diminished, and dysregulated. (A–C)** Groups of adult or aged (10-wk- or 40-wk-old) C57BL/6 mice (n = 3–5 per group) were infected with 300 PFU MA20. Lungs were harvested at the indicated time points, processed, and subjected to RNA-sequencing. **(A)** Principal component analysis plot of RNA-sequencing data obtained from total lungs of the indicated groups of mice. **(B)** GSEA comparing adult and aged mice at each time point after infection. Gene set preranked analyses were carried out using the C5 GO gene set collection in the Molecular Signatures Database. **(C)** Heat map for significant differences in canonical pathways as defined by IPA. Six pairwise comparisons between infected lung samples and their respective mock controls, from adult or aged animals, at the indicated days p.i., are shown (fold change >1.5, padj <0.05). The Benjamini–Hochberg method of multiple testing correction was used to calculate –log(P values). Up- and down-regulated transcripts across the different pairwise comparisons in the "Th1 and Th2 pathway" are shown as heat maps.

Ifnar1$^{-/-}$*Ifnlr1*$^{-/-}$ mice compared with their respective adult controls (Fig. 6, B–E). These results indicated that individual or combinatorial loss of type I and type III IFN signaling in adult mice does not recapitulate the pathomechanism leading to the increased disease severity observed in aged WT mice. Since GSEA and IPA of SARS-CoV-2–infected lung samples both identified an age-dependent reduction in the IFN-γ–mediated immune response to infection, we also assessed the contribution of an impaired type II IFN response to the age-related phenotype. Interestingly, weight loss of adult *Ifngr1*$^{-/-}$ mice within the first 4 d of infection was comparable with that of aged *Ifngr1*$^{-/-}$ mice (Fig. 6 F). This is in contrast to the comparison of aged versus adult WT, *Ifnar1*$^{-/-}$, *Ifnlr1*$^{-/-}$, and *Ifnar1*$^{-/-}$*Ifnlr1*$^{-/-}$ mice (Fig. 6, B–E). In these genotypes, a marked weight loss within 4 d p.i. was only observed in aged but not adult mice. The loss of age-dependent differences during the first days of infection in *Ifngr1*$^{-/-}$ mice supports our previous findings obtained by transcriptional profiling (Figs. 1 H and 5, B and C), which suggested a relevant contribution of an early and potent IFN-γ response to prevent SARS-CoV-2–induced disease in adult mice. However, aged *Ifngr1*$^{-/-}$ mice still showed enhanced disease progression and increased lethality compared with adult *Ifngr1*$^{-/-}$ controls (Fig. 6 F), suggesting an age-related impairment of additional factors that may contribute to enhanced disease severity in aged *Ifngr1*$^{-/-}$ mice. To test if the production of type I and III IFNs or the response to type I IFNs might be compromised in the aged host, we intranasally treated adult and aged *Ifnlr1*$^{-/-}$ mice with poly (I:C), a synthetic analog of double-stranded RNA, and measured the mRNA expression levels of IFN-β (type I IFN), IFN-λ (type III IFN), and two representative ISGs in their lungs. Although the expression levels of *Ifnl2/3* transcripts did not differ between adult and aged mice, we found

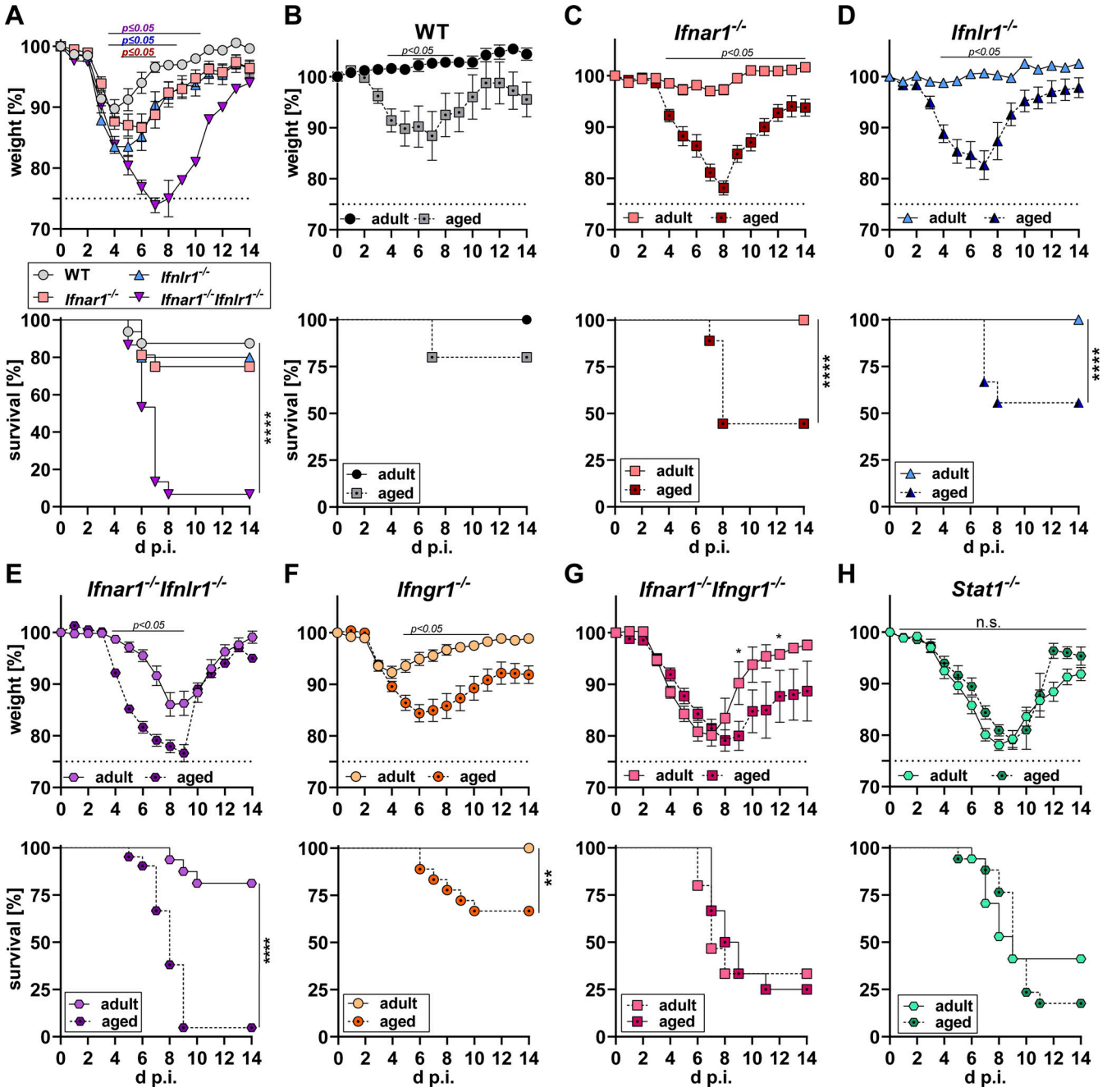

Figure 6. **Combined deficiency in type I and type II IFN signaling phenocopies age-dependent disease susceptibility. (A)** Adult (8–20-wk-old) WT, *Ifnar1*$^{-/-}$, *Ifnlr1*$^{-/-}$ and *Ifnar1*$^{-/-}$*Ifnlr1*$^{-/-}$ mice (n = 15–16) were infected with 300 PFU MA20. Weight loss (upper panel) and survival (lower panel) were monitored for 14 d p.i. Data pooled from two independent experiments. Dashed line indicates experimental endpoint due to animal welfare. Symbols represent mean ± SEM. Weight loss: P values for WT in comparison with *Ifnar1*$^{-/-}$ (red), *Ifnlr1*$^{-/-}$ (blue), and *Ifnar1*$^{-/-}$*Ifnlr1*$^{-/-}$ (purple) by two-way ANOVA with Tukey's multiple comparisons test. Survival: ****P ≤ 0.0001, Log-rank (Mantel-Cox) test. **(B–H)** Groups of adult or aged (10–20-wk- or 38–60-wk-old) mice of the indicated genotypes were infected with 30 PFU MA20. Weight loss (upper panel) and survival (lower panel) were monitored for 14 d p.i. Dashed line indicates experimental endpoint due to animal welfare. Weight loss: P values calculated by two-way ANOVA with Šídák's multiple comparisons test, *P ≤ 0.05. Survival: **P ≤ 0.01, ****P ≤ 0.0001, Log-rank (Mantel-Cox) test. **(B–D)** All mice were infected in parallel, and data from a single experiment are shown; n = 5–9. **(E)** Data pooled from two independent experiments; n = 17–21. **(F)** Data pooled from three independent experiments; n = 18–20. **(G)** Data pooled from two independent experiments; n = 11–15. **(H)** Data pooled from two independent experiments; n = 17.

a significantly reduced induction of *Ifnb1* expression in aged mice upon poly (I:C) treatment (Fig. S3 B). Similarly, expression levels of *Mx1* and *Isg15* were significantly lower in lungs of aged *Ifnlr1*$^{-/-}$ mice compared with adult controls, at baseline as well as upon poly (I:C) stimulation (Fig. S3 B). Consistent with the age-dependent decrease in type I IFN production and impaired IFN-γ–mediated response, we found that virus-induced weight loss and survival rates of adult mice lacking type I and type II IFN

receptors (*Ifnar1*$^{-/-}$*Ifngr1*$^{-/-}$) were nearly identical to that of aged controls (Fig. 6 G). In addition, adult *Stat1*-deficient mice lacking the ability to respond to any type of IFN were also equally susceptible to SARS-CoV-2–induced disease and lethality as their aged counterparts (Fig. 6 H).

Collectively, these data suggested that excessive virus replication promoted by impaired type I IFN system in combination with impaired IFN-γ–mediated immune responses can account for the observed high SARS-CoV-2 disease susceptibility of aged mice.

Therapeutic administration of IFN-λ prevents SARS-CoV-2–induced lethality and supplementation of IFN-γ reverses the age-dependent disease phenotype

Experiments using *Ifnar1*$^{-/-}$ and *Ifnar1*$^{-/-}$*Ifnlr1*$^{-/-}$ mice demonstrated that endogenously produced type III IFNs can partially substitute for a dysfunctional type I IFN immunity (Bastard et al., 2021; Bastard et al., 2020; Zhang et al., 2020), thereby protecting against lethal disease progression (Fig. 6 A). Therefore, we evaluated the antiviral potential of IFN-λ as a drug candidate (Feld et al., 2021) in the context of dysfunctional type I IFN immunity. Prophylactic administration of 2 µg IFN-λ1/3 (Yu et al., 2016) 1 d prior to infection or a therapeutic regimen of 3 µg per day for 1 wk starting 1 d after infection efficiently prevented lethal disease progression in adult *Ifnar1*$^{-/-}$ mice (Fig. 7 A). As certain monogenetic defects (Zhang et al., 2020) and autoantibodies (Wang et al., 2021) could also affect the protective effects of type III IFNs, we also tested prophylactic administration of IFN-$\alpha_{B/D}$ in adult *Ifnlr1*$^{-/-}$ mice. IFN-$\alpha_{B/D}$ treatment was similarly protective against lethal diseases as IFN-λ administration in absence of a functional type I IFN immunity (Fig. S4 A). Modeling advanced age in combination with dysfunctional type I IFN immunity by using aged *Ifnar1*$^{-/-}$ mice, we found that prophylactic administration of IFN-λ was not sufficient to significantly reduce disease burden in such highly susceptible mice (Fig. 7 B), whereas therapeutic administration of IFN-λ showed some residual protective activity by significantly reducing weight loss with a trend toward increased survival rates (Fig. 7 B). Of note, therapeutic application of IFN-λ efficiently protected aged WT animals with functional type I IFN immunity against SARS-CoV-2 induced lethal disease (Fig. S4 B) and efficiently reduced viral replication in upper airways and lungs (Fig. S4 C). Next, we treated aged WT mice daily with 2 µg IFN-γ from −1 to 7 d p.i. to test whether supplementation of IFN-γ could reverse the age-dependent enhanced disease severity upon SARS-CoV-2 infection. Infection with 200 PFU MA20 caused substantial weight loss and lethal disease progression in five out of eight aged WT mice, whereas aged WT mice supplemented with IFN-γ showed significantly reduced weight loss and an increased survival rate which was nearly identical to the disease course of adult WT mice (Fig. 7 C). In line, virus replication in the lungs of aged WT mice was effectively reduced by IFN-γ administration (Fig. 7 D). Encouraged by the positive results of IFN-λ in adult *Ifnar1*$^{-/-}$ and those of IFN-γ in aged WT animals, we next tested a combination of both treatments in an attempt to protect highly susceptible aged mice with a defective type I IFN system. Although individual therapeutic treatment regimens with either IFN-λ or IFN-γ in aged *Ifnar1*$^{-/-}$ both conferred only limited protection against SARS-CoV-2 induced disease and lethality (Fig. 7 B and Fig. S4 D), the combinatorial therapeutic treatment with IFN-λ1/3 and IFN-γ prevented morbidity exceeding 10% of body weight loss in an otherwise lethal infection (Fig. 7 E) and significantly reduced viral replication in upper airways and lungs (Fig. 7 F).

Taken together, these data demonstrated that (i) the drug candidate IFN-λ1/3 could efficiently prevent lethal disease progression in adult mice with defective type I IFN immunity, (ii) supplementation of IFN-γ could reverse the age-dependent enhanced disease progression, and (iii) the combination of both treatments rescued lethally infected aged mice lacking type I IFN responses (Fig. S5).

Discussion

Two major risk factors for severe COVID-19 are advanced age (O'Driscoll et al., 2021) and impaired IFN-mediated immunity (Zhang et al., 2020; Bastard et al., 2020; Bastard et al., 2021). For the rational design of effective therapeutics and prevention strategies targeting the respective risk groups, a better understanding of the disease-causing mechanisms is urgently needed. Small animal models faithfully recapitulating characteristics of human disease are pivotal to overcome these limitations. In this study, we generated a highly pathogenic mouse-adapted SARS-CoV-2 variant that can be used to model mild, moderate, or severe COVID-19 in standard inbred C57BL/6 mice. Our model recapitulates several findings observed in COVID-19 patients, such as ACE2-dependent infection of bronchial and alveolar epithelial cells, including type 2 pneumocytes, causing viral pneumonia. This may result in severe disease, which is associated with a prominent cytokine production resembling severe COVID-19 in patients (Lucas et al., 2020; Sposito et al., 2021). Importantly, our infection model in mice faithfully reflects the age-dependent disease aggravation observed in humans. The histopathologic changes observed in our model mimic some aspects of the overall heterogenous picture of human COVID-19, including early viral pneumonia with alveolar epithelial necrosis, vascular endothelial activation with leukocyte rolling, and, in some cases, vascular endotheliitis and formation of atypical multinucleated giant cells. As expected, several aspects of human COVID-19, such as diffuse alveolar damage with hyaline membrane formation or microthrombosis, were absent in our model, which was evaluated up to day 7 p.i. However, human histological data are almost exclusively from autopsies and are thus based on fatal disease courses and/or from patients with significant comorbidities (Caramaschi et al., 2021; Pannone et al., 2021).

Using this small animal model, we found that the age-dependent increase in disease severity is driven by an impaired interferon response which causes delayed, insufficient, and dysregulated innate and adaptive immune response in the aged host. Transcriptome analyses of infected lungs from mature adult and middle-aged C57BL/6 mice revealed that adult mice initiated a rapid and well-coordinated innate and adaptive immune response, which was associated with high IFN-γ and low IL-10 expression levels. This effective and timely immune

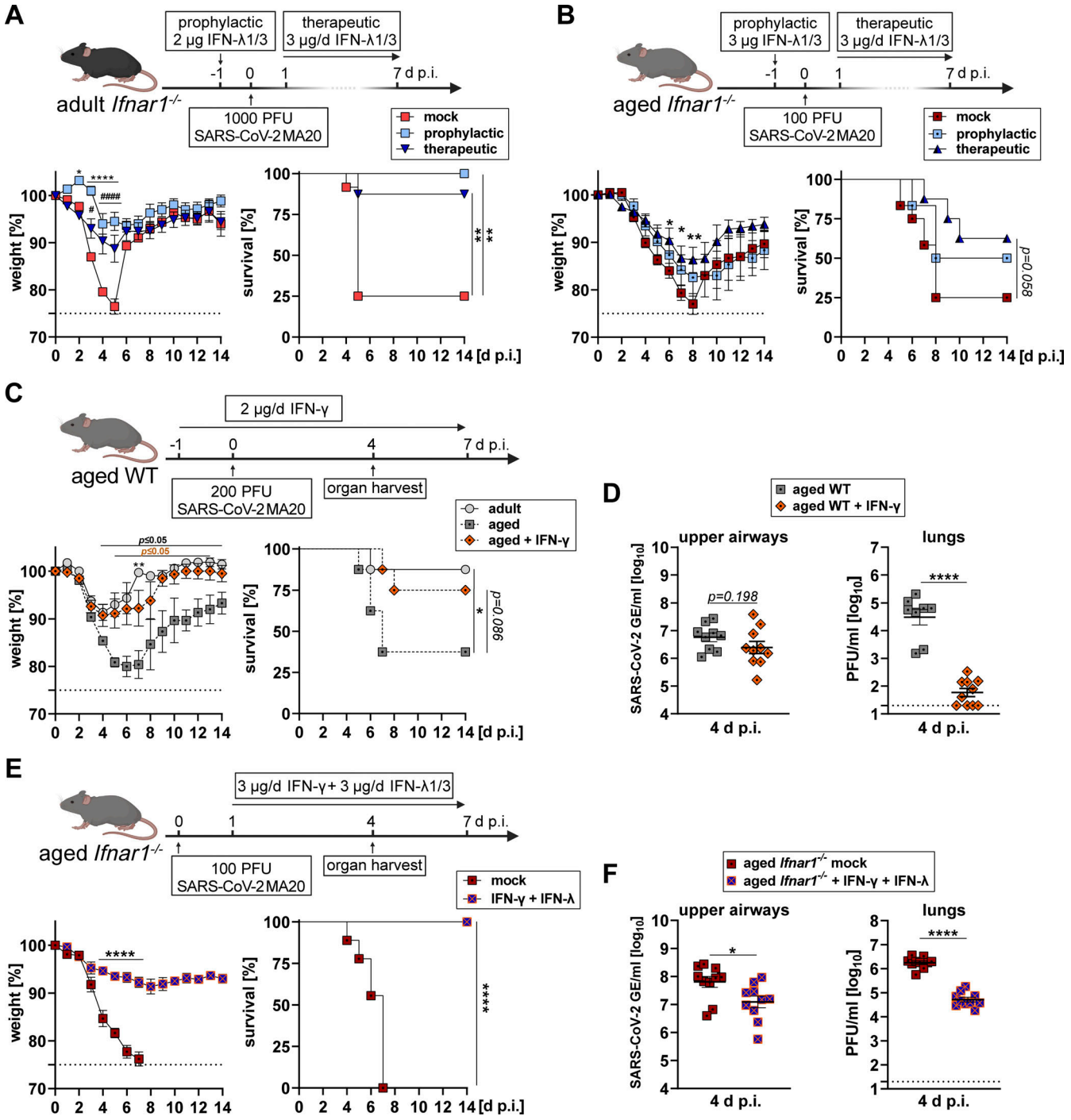

Figure 7. **Therapeutic administration of IFN-λ prevents SARS-CoV-2–induced lethality in absence of type I IFN immunity and supplementation of IFN-γ reverses age-dependent disease phenotype. (A)** Groups of adult *Ifnar1*$^{-/-}$ mice (9–15-wk-old) were either mock-treated (n = 12), treated prophylactically by subcutaneous injection of 2 µg IFN-λ1/3 once 1 d prior to infection (n = 6), or treated therapeutically with 3 µg IFN-λ1/3 daily for 1 wk (n = 8) starting 1 d after infection with 1,000 PFU MA20. Dashed line indicates experimental endpoint due to animal welfare. Pooled data from two independent experiments are shown. Symbols represent mean ± SEM. Weight loss: mock in comparison with prophylactic (asterisks) or therapeutic (hashes) by two-way ANOVA with Tukey's multiple comparisons test; *P ≤ 0.05, #P ≤ 0.05, ****P ≤ 0.0001, ####P ≤ 0.0001. Survival: Log-rank (Mantel-Cox) test; **P ≤ 0.01. **(B)** Groups of aged *Ifnar1*$^{-/-}$ (49–60-wk-old) mice were either mock-treated (n = 12), treated prophylactically by subcutaneous injection of 3 µg IFN-λ1/3 once 1 d prior to infection (n = 6), or treated therapeutically with 3 µg IFN-λ1/3 daily for 1 wk (n = 8) starting 1 d after infection with 100 PFU MA20. Dashed line indicates experimental endpoint due to animal welfare. Pooled data from two independent experiments are shown. Symbols represent mean ± SEM. Weight loss: mock in comparison with therapeutic by two-way ANOVA with Tukey's multiple comparisons test; *P ≤ 0.05, **P ≤ 0.01. Survival: Log-rank (Mantel–Cox) test. **(C)** Groups of aged WT mice (45–52-wk-old) were either mock-treated (n = 8) or treated subcutaneously with 2 µg IFN-γ daily (n = 8) for 9 d starting 1 d prior to infection with 200 PFU MA20. Infected but untreated adult WT mice (10–16-wk-old; n = 8) served as controls. Dashed line indicates experimental endpoint due to animal welfare. Data from a single experiment are shown. Symbols represent mean ± SEM. Weight loss: P ≤ 0.05 for mock-treated aged mice in comparison with adult control mice (black) or with IFN-γ–treated aged mice (orange) by two-way ANOVA with Tukey's multiple comparisons test; **P ≤ 0.01

comparing adult control mice with IFN-γ–treated aged mice. Survival: Log-rank (Mantel-Cox) test, *P ≤ 0.05. **(D)** Groups of aged WT mice (55–60-wk-old; *n* = 9–10) were treated and infected as depicted in C. Organs were harvested on day 4 p.i. Viral replication in upper airways was quantified as SARS-CoV-2 genome equivalents per ml by measuring expression levels of the viral gene *E* by RT-qPCR. Lung (left panel) and viral loads in lungs were determined by plaque assay on Vero E6 cells (right panel). Symbols represent individual mice and bars indicate mean ± SEM. ****P ≤ 0.001, unpaired *t* test. **(E)** Groups of aged *Ifnar1*$^{-/-}$ mice (52–60-wk-old) were either mock-treated (*n* = 9) or treated therapeutically with a mixture of 3 µg IFN-λ1/3 and 3 µg IFN-γ daily for 1 wk (*n* = 8), starting 1 d after infection with 100 PFU MA20. Dashed line indicates experimental endpoint due to animal welfare. Data from a single experiment are shown. Symbols represent mean ± SEM. Weight loss: mock in comparison with therapeutic treatment group by two-way ANOVA with Šídák's multiple comparisons test; ****P ≤ 0.0001. Survival: Log-rank (Mantel-Cox) test; ****P ≤ 0.0001. **(F)** Groups of aged *Ifnar1*$^{-/-}$ mice (53–60-wk-old; *n* = 10) were treated and infected as depicted in (E). Organs were harvested on day 4 p.i. Viral replication in upper airways was quantified as SARS-CoV-2 genome equivalents per ml by measuring expression levels of the viral gene *E* by RT-qPCR. Lung (left panel) and viral loads in lungs were determined by plaque assay on Vero E6 cells (right panel). Symbols represent individual mice and bars indicate mean ± SEM. *P ≤ 0.05, ****P ≤ 0.001, unpaired *t* test.

response in adults limited viral loads, mediated rapid viral clearance, and efficiently prevented the development of severe disease. In aged mice, by contrast, virus replication was markedly increased, which correlated with the absence of effective antiviral immune responses. Instead, aged mice showed strong IL-6– and IL-1–mediated responses associated with low IFN-γ and high IL-10 expression levels. The markedly different IFN-γ to IL-10 ratio likely explains the effective immune response, including NK cell–mediated immunity, efficient antigen presentation, lymphocyte activation, and immunoglobulin production in adult mice that leads to the favorable disease outcome compared with aged counterparts (Fig. S5).

Interestingly, in spite of the enhanced disease progression in aged animals, lung tissue damage was comparable between both age groups at the time points investigated. However, in aged animals, we observed a widespread viral infection of alveolar epithelial cells, whereas in adult animals infection was mainly confined to peribronchial areas. It is tempting to speculate that the diffuse and widespread infection of the aged lung may lead to a functional impairment of the respiratory system even before excessive cellular damage is detectable by classical histological methods, such as H&E staining. A limitation of our study is that we could not perform pulmonary function tests or live imaging of infected mice using techniques like micro–computed tomography, which may allow for a better comparison with humans. Besides severely impaired respiratory function, it is possible that aged mice suffered from a systemic manifestation of disease due to overshooting cytokine production (Karki and Kanneganti, 2021) or virus dissemination to other organs. Indeed, quantitative RT-qPCR analyses revealed elevated viral RNA levels in both heart and brain samples of aged mice. However, neither signs of inflammation or immune cell infiltrations were detected nor were viral RNA-positive cells found in heart and brain samples from aged mice using highly sensitive RNA ISH methods, arguing against a substantial systemic dissemination of the virus in aged animals.

To test whether an impaired IFN response would indeed phenocopy the enhanced disease progression in the aged host, we directly compared adult and aged mice with individual or combinatorial deficiencies in the various IFN pathways. We found that type I and type III IFNs limited disease susceptibility and lethality, but genetic defects in these pathways did not faithfully recapitulate the age-dependent enhanced disease phenotype. Importantly, however, adult *Ifngr1*$^{-/-}$ mice with a deficient type II IFN system suffered from increased disease severity that closely resembled the disease course of aged WT mice. Nevertheless, aged *Ifngr1*$^{-/-}$ mice still showed enhanced disease progression and increased lethality compared with their younger counterparts, indicating that additional mechanisms are also involved in the age-dependent disease severity. In line with an age-dependent reduction in type I IFN production upon stimulation with poly (I:C), adult *Ifnar1*$^{-/-}$*Ifngr1*$^{-/-}$ mice lacking functional type I and type II IFN signaling indeed showed the same degree of severe weight loss and poor survival rates as their aged counterparts. These results demonstrate a defining role of diminished type I and type II IFN responses in driving the age-dependent virulence of SARS-CoV-2.

We, therefore, hypothesize that the age-dependent impairment of IFN-γ–mediated responses causes the impaired NK cell activation, reduced antigen presentation, and diminished lymphocyte activation that we see in our transcriptome data, whereas the impaired type I IFN immunity facilitates virus replication due to reduced cell-intrinsic antiviral immunity. In agreement with our finding that adult *Ifngr1*$^{-/-}$ mice phenocopied the disease course of aged WT animals, we found that treatment of aged mice with IFN-γ prevented severe disease progression, supporting the view that IFN-γ limits age-dependent COVID-19 severity. By comparing children and adults, other researchers found that increased expression levels of PRRs such as MDA5 and RIG-I maintain a tonic IFN-activated antiviral state in the airways which appears to contribute to the high resistance of young individuals against severe COVID-19 (Loske et al., 2021; Yoshida et al., 2021). Consistent with this, we find an age-dependent reduction of baseline ISG expression in the lungs of aged mice due to impaired type I IFN production. However, it is unclear whether such mechanisms, which may explain the elevated baseline of type I and type III IFNs, would affect IFN-γ production. Whereas type I and type III IFNs are produced mainly by dendritic cells as well as infected epithelial cells upon activation of PRRs (Paludan and Mogensen, 2022), IFN-γ is mainly produced by NK and T cells and involves distinct transcription factors such as Eomes and T-bet in its regulation (Fenimore and Young, 2016). Of note, adult mice in our study showed significantly increased expression levels of T-bet in their infected lungs compared with aged mice.

Additional studies are required to determine which pathways and cell types are involved in the detection of SARS-CoV-2 infection, and which cells produce the respective types of interferon to prevent severe disease. The identification of cell types that fail to produce IFN-γ and/or fail to adequately respond to

this cytokine in the aged organism may enable the development of novel strategies that aim at preventing or reversing such pathological processes. A recent study showed that soluble factors in plasma from severe COVID-19 patients reversibly interfered with the antiviral activity of NK cells and their capacity to mount an appropriate IFN-γ and TNF response that otherwise was associated with a favorable disease outcome (Krämer et al., 2021). Interestingly, others suggested a potential disease-driving role of IFN-γ in combination with TNF, possibly inducing inflammatory cell death during severe COVID-19 via PANoptosis (Karki et al., 2021). However, we observed that the protective effects of endogenous or exogenous IFN-γ during SARS-CoV-2 infection clearly outweigh possible detrimental effects in our infection model. These contrasting findings emphasize the potential duality of some cytokines such as IFNs and TNF that are essential to confer immunity against infection but may have the potential to augment disease progression, often due to a dysregulation of timing and location (Sposito et al., 2021; Lucas et al., 2020).

Similarly, two recent studies raised awareness that continuous IFN-λ signaling could hamper efficient lung repair after viral infection (Broggi et al., 2020; Major et al., 2020). However, in our COVID-19 mouse model, IFN-λ deficiency led to increased and prolonged viral replication causing enhanced disease and delayed recovery. Vice versa, both prophylactic and therapeutic treatment with IFN-λ strongly reduced viral loads in the lung and efficiently prevented disease deterioration in lethally infected aged mice or adult animals lacking type I IFN immunity. This strongly indicates that the protective effects of IFN-λ during severe SARS-CoV-2 infections outcompete potential adverse effects. Notably, individual therapeutic treatment of infected aged *Ifnar1*$^{-/-}$ mice, a model combining two of the most detrimental risk factors for severe COVID-19 in humans (O'Driscoll et al., 2021; Bastard et al., 2021), with either IFN-γ or IFN-λ had limited success in preventing severe disease and lethality. However, the combination of both cytokines proved to be highly efficient. We, therefore, hypothesize that exogenous IFN-γ rescues the age-related impairment of cellular immune responses, whereas IFN-λ compensates for the compromised cell-intrinsic antiviral immunity in epithelial cells. Both cytokines may also improve DC migration into draining lymph nodes facilitating T cell activation (Ye et al., 2019a), a process which is impaired in infected aged mice due to elevated levels of prostaglandin D_2 and its upstream phospholipase PLA2G2D (Wong and Perlman, 2022; Vijay et al., 2015; Zhao et al., 2011; Wong et al., 2022). Interestingly, such elevated PGD_2 levels may also drive enhanced disease by interfering with the production of IFN-λ (Werder et al., 2018). Both IFN-γ and IFN-λ treatments were already evaluated in various clinical settings. IFN-γ is licensed to treat chronic granulomatous disease (Todd and Goa, 1992) and is discussed as a treatment for idiopathic pulmonary fibrosis (Smaldone, 2018). IFN-λ treatment was well tolerated by patients in the context of hepatitis C virus infections (Muir et al., 2010; Andersen et al., 2013; Nelson et al., 2017), and a recent clinical trial demonstrated a marked efficacy in accelerating viral decline and clearance in SARS-CoV-2 infected patients (Feld et al., 2021). Given the ongoing burden of the current and the threat of future pandemics, it should be considered whether the clinical use of broad-spectrum antivirals such as type II and type III interferons could prevent exacerbation of SARS-CoV-2 induced disease in patients while possibly also mitigating virus transmission.

Material and methods

Viruses and cell lines

The virus strain SARS-CoV-2 MA containing the amino acid changes Q498Y and P499T in the spike protein (Dinnon et al., 2020) has been generated by transformation-associated recombination in yeast as previously described (Thi Nhu Thao et al., 2020). Briefly, the mutations resulting in the Q498Y and P499T amino acid changes in the spike protein were generated in plasmids containing fragments 9 and 10 by using primers mSARSv3Fg9+10-F (5′-ATATGGTTTCTACACGACTAATGGTGT TGGTTAC-3′) and mSARSv3Fg9+10-R (5′-GATTGTAAAGGA AAGTAACAATTAAAAC-3′) by Q5 site-directed mutagenesis (New England Biolabs). Passage one SARS-CoV-2 MA stocks produced using Vero E6 cells were used in experiments. The identity of the resulting recombinant SARS-CoV-2 MA was confirmed by sequencing.

PP virus stocks from passage 20 lung homogenates of passaging series DKO A and B were grown using Vero E6 cells. PP virus stock derived from passaging series DKO A was plaque-purified a second time using Vero E6 cells to generate an MA20 virus stock for experiments. Briefly, virus stocks were produced by inoculating confluent Vero E6 cells with virus diluted in Opti-MEM (Gibco) 0.3% BSA (Sigma-Aldrich) for 2 h at 37°C with 5% CO_2 after removal of cell culture medium (DMEM [Gibco] containing 10% FCS [Anprotec], 20 U/ml penicillin, and 20 µg/ml streptomycin [Gibco]) and washing with PBS. After removal of infection medium, cells were washed with PBS and DMEM containing 2% FCS, and 20 mM Hepes (Roth) was added. After incubation for 48–72 h at 37°C with 5% CO_2, cell culture supernatants were harvested, cleared by centrifugation, aliquoted, and stored at −80°C until further use. Viral load in virus stocks was determined by plaque assay using Vero E6 cells. Purity of virus stocks was confirmed by next-generation sequencing.

Sequenced B.1 (Muc-IMB-1/2020) and B.1.617.2 (Delta) virus stocks were provided by Georg Kochs (Kaleta et al., 2022).

African green monkey kidney Vero E6 cell line (ATCC CRL-1586) and human lung adenocarcinoma Calu-3 cell line (ATCC HTB-55) were purchased from ATCC. All virus infection experiments were performed under BSL-3 conditions.

Mice

C57BL/6JRj, BALB/cJRj, and 129S2/SvPasOrlRj mice were purchased from Janvier Labs. B6.A2G-*Mx1*, B6.A2G-*Mx1-Ifnar1*$^{-/-}$, B6.A2G-*Mx1-Ifnlr1*$^{-/-}$, B6.AG2-*Mx1-Ifnar1*$^{-/-}$*Ifnlr1*$^{-/-}$, B6.*Ifngr1*$^{-/-}$, B6.*Ifnar1*$^{-/-}$*Ifngr1*$^{-/-}$, and B6.A2G-*Mx1-Stat1*$^{-/-}$ were bred and kept at the animal facilities of the University Medical Center Freiburg.

Mature adult 8–20-wk-old mice, designated "adult," and middle-aged 36–60-wk-old mice, designated "aged," were used in experiments. Animals of both sexes were used. All experimental groups were sex- and age-matched.

Infection of mice, IFN treatments, and poly (I:C) stimulation

Mice were anesthetized using 1.8–2.8 vol % isoflurane in O_2 and subsequently inoculated with 40 µl PBS 0.1% BSA containing the indicated dose of the respective virus variant via their nostrils. Infected mice were monitored daily for weight loss and clinical signs of disease for at least 2 wk. Experimental endpoints when mice were euthanized by cervical dislocation were defined as ≥25% weight loss or ≥20% weight loss for longer than 2 d.

Poly (I:C) (P0913; Sigma-Aldrich; 1 mg/ml) was administered intranasally to isoflurane-anesthetized mice in a 40 µl volume. To collect organ samples, mice were euthanized by cervical dislocation. For histopathological analyses, mice were anesthetized using ketamine/xylazine, fixed by transcardial perfusion with 10% formalin solution, and stored in 10% formalin solution at 4°C until further processing.

To determine viral loads by plaque assay, organs were homogenized three to four times in 800 µl PBS at 6.5 m/s for 18 s using a FastPrep tissue homogenizer (MP Biomedicals). Homogenates were centrifuged at 10,000 rpm for 10 min and the supernatants were collected and stored at −80°C until further processing.

Nasal swabs were collected using a wet cotton swab and stored in 650 µl Opti-MEM 0.3% BSA at −80°C. Samples were thawed at 20°C with 1,400 rpm for 15 min on a thermoshaker and viral load determined by plaque assay.

For intranasal treatment, isoflurane-anesthetized mice were mock-treated with PBS 0.1% BSA or inoculated with the respective doses of IFN-$\alpha_{B/D}$ (Horisberger and de Staritzky, 1987) or human IFN-λ1/3 (Yu et al., 2016) in a 40-µl volume via their nostrils.

For subcutaneous treatment, mice were mock-treated with PBS 0.1% BSA or injected with the respective doses of human IFN-$\alpha_{B/D}$, IFN-λ1/3 or mouse IFN-γ, or a combination of both in a 100 µl volume using a 30-G syringe.

Plaque assay

10-fold serial dilutions of infectious samples were prepared in Opti-MEM 0.3% BSA and added to PBS-washed confluent Vero E6 cells, incubated for 2 h at 37°C with 5% CO_2 before inoculum was removed, and cells overlaid with DMEM containing 0.1% BSA, 1.5% Avicel (FMC BioPolymer), 0.5 mg/ml L-glutamine (Roth), 20 mM Hepes, 20 U/ml penicillin, and 20 µg/ml streptomycin and incubated for 72 h at 37°C with 5% CO_2. After removal of Avicel medium, cells were fixed using 10% formalin solution and stained with 1% crystal violet in H_2O containing 20% ethanol, each step for at least 25 min. Plaques were counted and used to calculate virus titers defined as PFU per ml.

To plaque-purify clonal isolates, cells infected with serial dilutions were overlaid with DMEM containing 2% FCS, 0.6% agar (Oxoid), 0.01% diethylaminoethyl (DEAE)-dextran (Sigma-Aldrich), and 0.1% $NaHCO_3$ (Merck), and plaques picked 48–72 h p.i. using a thin filter-tip containing 2 µl PBS.

Cell culture, virus growth curves, and plaque reduction neutralization test

Vero E6 and Calu-3 cells were cultured in DMEM and MEM, respectively, containing 10% FCS, 20 units/ml penicillin, and 20 µg/ml streptomycin.

For virus growth curves, Vero E6 or Calu-3 cells were seeded in 24-well plates, and after washing with PBS, infected with the respective virus strain by incubating the cells with virus containing Opti-MEM 0.3% BSA for 2 h at 37°C with 5% CO_2 using a multiplicity of infection (MOI) of 0.001. Cells were then cultured in DMEM containing 2% FCS, after washing with PBS. Cell culture supernatants were collected at the indicated time points and viral loads were determined by plaque assay on Vero E6 cells.

Serological neutralization tests were performed using sera from vaccinated individuals 10–25-wk after vaccination with the second dose of Comirnaty (BioNTech/Pfizer) or Spikevax (Moderna). Serial twofold dilutions of sera in Opti-MEM 0.3% BSA were incubated for 1 h with 100 PFU of the indicated SARS-CoV-2 variant. The mixture was then added to Vero E6 cells and incubated for 1.5 h at 37°C with 5% CO_2. After removal of the inoculum, cells were overlaid with DMEM containing 2% FCS, 0.6% agar, 0.01% DEAE-dextran, and 0.1% $NaHCO_3$ and incubated for 72 h at 37°C with 5% CO_2. Cells were fixed for 20 min using 10% formalin solution, stained for 20 min with 1% crystal violet in H_2O containing 20% ethanol, and plaques were counted. Plaque reduction was calculated relative to mock-treated controls. 50% neutralizing titers were calculated by nonlinear fit least squares regression (constraints: 0 and 100).

RNA isolation and RT-qPCR

For RNA isolation, organ samples were homogenized four times in 800 µl TRI Reagent (Zymo Research Corporation) at 6.5 m/s for 20 s using a FastPrep tissue homogenizer (MP Biomedicals). Samples were centrifuged at 10,000 rpm for 5 min, and supernatant diluted in TRI Reagent (1:2 to 1:32) was used for RNA extraction using the Direct-zol RNA Miniprep kit according to the manufacturer's instructions (Zymo Research Corporation).

cDNA was reverse-transcribed from 750 ng total RNA per sample using the LunaScript RT SuperMix kit (New England Biolabs) and served as a template for amplification of genes of interest (*Ubc*, QuantiTect Primer Assay, Cat. No. QT00245189; *Tnf*, QuantiTect Primer Assay, Cat. No. QT00104006; *Ifna4*, QuantiTect Primer Assay, Cat. No. QT01774353; *Ifnl2/3*, Applied Biosystems, Cat. No. mm0420156_gH; *Ifnb1*, forward: 5′-CCT GGAGCAGCTGAATGGAA-3′, reverse: 5′-CACTGTCTGCTGGTG GAGTTCATC-3′, probe: 5′-[6FAM]CCTACAGGGCGGACTTCAAG [BHQ1]-3′; *Isg15*, forward: 5′-GAGCTAGAGCCTGCAGCAAT-3′, reverse: 5′-TTCTGGGCAATCTGCTTCTT-3′; *Stat1*, forward: 5′-TCACAGTGGTTCGAGCTTCAG-3′, reverse: 5′-CGAGACATCATA GGCAGCGTG-3′; *Mx1*, forward: 5′-TCTGAGGAGAGCCAGACG AT-3′, reverse: 5′-ACTCTGGTCCCCAATGACAG-3′; *Il6*, forward: 5′-TCGGAGGCTTAATTACACATGTTCT-3′, reverse: 5′-GCATCA TCGTTGTTCATACAATCA-3′) using SYBR Green PCR Master Mix (Applied Biosystems) or TaqMan Universal PCR Master Mix (Qiagen) and a QuantStudio 5 Real-Time PCR System (Applied Biosystems). The increase in mRNA expression was determined by the $2^{-\Delta Ct}$ method relative to the expression of the indicated housekeeping gene.

Viral RNA was quantified by one-step RT-qPCR using the AgPath-ID One-Step RT-PCR (Applied Biosystems) reagents and the 2019-nCoV RT-qPCR primers (E_Sarbeco; Corman et al.,

2020) specific for the viral E gene. Serial dilutions of a defined RNA standard were used for absolute quantification as previously described (Schlottau et al., 2020).

Virus genome sequencing

RNA was extracted from 50 µl lung homogenate supernatant using the NucleoSpin RNA Mini Kit according to the manufacturer's protocol (MACHEREY-NAGEL). cDNA was reverse-transcribed from extracted RNA using random hexamer primers and Superscript III (Thermo Fisher Scientific) followed by PCR tiling of the entire SARS-CoV-2 genome (ARTIC V3 primer sets; https://github.com/artic-network/artic-ncov2019) producing ∼400-bp-long overlapping amplicons that were used to prepare the sequencing library. Amplicons were purified with AMPure magnetic beads (Beckman Coulter), and QIAseq FX DNA Library Kit (Qiagen) was used to prepare indexed paired-end libraries for Illumina sequencing. Normalized and pooled sequencing libraries were denatured with 0.2 M NaOH. Libraries were sequenced on an Illumina MiSeq using the 300-cycle MiSeq Reagent Kit v2.

Demultiplexed raw reads were subjected to a customized Galaxy pipeline based on bioinformatics pipelines on https://usegalaxy.eu/ (Kumar et al, 2020). Raw reads were pre-processed with fastp v.0.20.1 (Chen et al., 2018) and mapped to the SARS-CoV-2 Wuhan-Hu-1 reference genome (Genbank: NC_045512) using BWA-MEM v.0.7.17 (Li and Durbin, 2009). Primer sequences were trimmed using ivar trim v1.9 (https://andersen-lab.github.io/ivar/html/manualpage.html). Variants (SNPs and INDELs) were called using the ultrasensitive variant caller LoFreq v2.1.5 (Wilm et al., 2012), demanding a minimum base quality of 30 and a coverage ≥10-fold. Called variants were filtered based on a minimum variant frequency of 10%. Effects of mutations were automatically annotated in vcf files using SnpEff v.4.3.1 (Cingolani et al., 2012). Consensus sequences were constructed using bcftools v.1.1.0 (Li et al., 2009). Regions with low coverage (>20-fold) or variant frequencies between 30 and 70% were masked with N.

A customized R script was used to plot variant frequencies that were detected by LoFreq as a heatmap (https://github.com/jonas-fuchs/SARS-CoV-2-analyses), which is also available on https://usegalaxy.eu/ ("Variant Frequency Plot").

RNA-sequencing

RNA was isolated from infected lungs as described above. RNA-sequencing was performed on the HiSeq 4000 system (Illumina) with Single End 75 bp reads. Read quality trimming and adaptor removal were carried out using Trimmomatic (version 0.36). The nf-core/rnaseq pipeline (version 3.0 [Ewels et al., 2020]) written in the Nextflow domain-specific language (version 19.10.0 [Di Tommaso et al., 2017]) was used to perform the primary analysis of the samples in conjunction with Singularity (version 2.6.0 [Kurtzer et al., 2017]). All data were processed relative to the mouse GRCm38 genome downloaded from Ensembl. Gene counts per gene per sample were obtained using the RSEM-STAR (Dobin et al., 2013; Li and Dewey, 2011) option of the pipeline, and they were imported on DESeq (v1.28.0 [Love et al., 2014]) within R environment v4.0.2 for differential expression analysis. Gene Ontology (GO) and GSEA was carried out using R package Cluster Profiler (v3.16). For GSEA, gene lists ranked using the Wald statistic were used. Preranked analyses were carried out using C5 ontology GO biological process gene sets from the Molecular Signatures database (MSigDB, v7.2). Gene signatures were considered significant if false discovery rate (FDR) q value ≤0.05. ggplot2, RColorBrewer, and ComplexHeatmap were used for plotting purposes. IPA was performed using differentially expressed genes (fold change ≥1.5, padj ≤0.05). The indicated –log(P values) were calculated using the Benjamini–Hochberg method of multiple testing correction.

Histopathology, IHC, RNA ISH, and scoring

Mice, after cardiac perfusion as described above, were immersion-fixed with 10% neutral-buffered formalin solution. Tissue was embedded in paraffin, including the whole lung, three to four trimmed sections of the decalcified nasal cavity, a sagittal section of the brain, and a longitudinal section of the heart. Samples were cut into 2–3-µm-thick sections and stained with H&E for light microscopical examination. Consecutive slides were processed for IHC. A polyclonal serum detecting the nucleocapsid protein of SARS-CoV-2 (# 200-401-A50; Rockland Immunochemicals) was used according to standardized procedures of the avidin–biotin–peroxidase complex-method (ABC, Vectastain Elite ABC Kit). Briefly, 2–3 µm sections were mounted on adhesive glass slides, dewaxed in xylene, followed by rehydration in descending graded alcohols. Endogenous peroxidase was quenched with 3% hydrogen peroxide in distilled water for 10 min at room temperature. Antigen heat retrieval was performed in 10 mM citrate buffer (pH 6) for 20 min in a pressure cooker. Nonspecific antibody binding was blocked for 30 min at room temperature using normal goat serum, diluted 1:2 in PBS. The primary polyclonal serum was applied overnight at 4°C (1:3,000, diluted in TRIS buffer) and the secondary biotinylated goat anti-rabbit antibody was applied for 30 min at room temperature (Vector Laboratories, 1:200). Color was developed by incubating the slides with freshly prepared avidin–biotin–peroxidase complex (ABC) solution (Vectastain Elite ABC Kit; Vector Laboratories), followed by exposure to 3-amino-9-ethylcarbazole substrate (Dako). Sections were counterstained with Mayer's hematoxylin and coverslipped. As negative control, a consecutive section was labeled with an irrelevant antibody detecting M protein of Influenza A virus (ATCC clone HB-64) and a positive control slide was included in each run.

To validate RT-qPCR data, selected tissues (heart and brain) were tested with RNA ISH. The RNAScope 2-5 HD Reagent Kit-Red (ACD, Advanced Cell Diagnostics) was used as previously published (Schlottau et al., 2020). For hybridization, RNAScope probes were custom-designed by ACD for SARS-CoV-2 nucleocapsid. The specificity of the probes was verified using a positive control probe detecting RNA encoding for peptidylprolyl isomerase B (cyclophilin B, ppib) and a negative control probe detecting RNA encoding for dihydrodipicolinate reductase. In addition, to identify subtle inflammation in brain and heart samples from infected 10-wk- (n = 10) and 40-wk-old (n = 6) C57BL/6, hearts were evaluated for the presence of CD3-positive T cell infiltrates and brains were evaluated for the presence of

CD3-positive T cells and Iba-1–positive microglial cells/macrophages, as described in Bennett et al. (2020).

All sides were scanned using a Hamamatsu S60 scanner and evaluation was done using NDPview.2 plus software (Version 2.8.24, Hamamatsu Photonics, K.K. Japan). The left lung lobe was evaluated for histological changes based on H&E staining applying criteria given in Table S1.

Following IHC, viral antigen was semiquantitatively recorded in the nasal cavity on ordinal scores using the tiers 0 = no antigen, score 1 = up to 3 foci, score 2 = >3 distinct foci, score 3 = coalescing foci, and score 4 = >80% antigen positive. The left lung lobe was evaluated using a 200 × 200 µm grid, positive grids were recorded, and the percentage of positive grids was calculated. Target cells were identified based on the cellular phenotype and their location as bronchial epithelium, alveolar macrophages, and alveolar epithelium, including type 1 and type 2 pneumocytes. For heart and brain samples, IHC-based antigen labeling as well as RNA ISH–based genome detection was recorded as present or absent.

Evaluation and interpretation were performed by a board-certified pathologist (DiplECVP) in a masked fashion using the postexamination masking method (Meyerholz and Beck, 2018).

Ethics and biosafety

The generation of recombinant SARS-CoV-2 MA was approved by the Swiss Federal Office for Public Health (permission A202819).

All work performed at the University Medical Center Freiburg concerning virus isolation, cell culture, and mouse infection experiments with infectious SARS-CoV-2 viruses were conducted in Biosafety Level 3 laboratories at the Institute of Virology, Freiburg, as approved by the Regierungspräsidium Tübingen (#UNI.FRK.05.16–31). All animal work conducted at the University Medical Center Freiburg and the Francis Crick Institute followed the German animal protection law or the Animals (Scientific Procedures) Act 1986, respectively, and was approved by the respective local animal welfare committee (Regierungspräsidium Freiburg #35–9185.81/G-20/91) or the UK Home Office London (Project Licence No. P9C468066). Animal infection experiments were performed consistent with procedures of the Federation for Laboratory Animal Science Associations and the national animal welfare body.

Human samples

Sera were obtained from eight vaccinees 10–25 wk after a second dose of the Comirnaty (BioN-TECH/Pfizer) or Spikevax (Moderna) vaccine. Written informed consent was obtained from participants, and the study was conducted according to federal guidelines and local ethics committee regulations (Albert-Ludwigs-Universität, Freiburg, Germany: No. F-2020-09-03-160428 and no. 322/20).

Statistical analyses

Data visualization and analyses were performed using GraphPad Prism 9.0 and R version 3.5.1. Specific statistical tests, numbers of animals and/or replicates, and further definitions of precision measures can be found in the respective figure legends or method details. P values are indicated in figures or figure legends.

Online supplemental material

Fig. S1 shows increased and prolonged replication of SARS-CoV-2 MA in mice lacking type I and/or type III IFN receptors. Fig. S2 shows serial passaging of MA SARS-CoV-2 in IFN receptor-deficient C57BL/6 mice allows for rapid host adaptation. Fig. S3 shows that increased disease susceptibility of aged mice is associated with an impaired type I IFN response. Fig. S4 shows that prophylactic IFN-α and therapeutic IFN-λ or IFN-γ treatment reduces SARS-CoV-2–induced lethality in highly susceptible mice. Fig. S5 shows that impaired immune response drives age-dependent virulence of SARS-CoV-2. Table S1 lists histological scoring criteria.

Material, data, and code availability

Material and reagents generated in this study will be made available upon installation of a Material Transfer Agreement. Virus genome sequences, including underlying raw data, have been deposited to the European Nucleotide Archive (https://www.ebi.ac.uk/ena/browser) under the study accession number ERA16794873. RNA sequencing data are available in GEO under accession code GSE190674.

Acknowledgments

We thank P. Staeheli for advice and constructive comments, and the animal-care technicians of the University Medical Center Freiburg for their excellent work and support. Illustrations were created with BioRender.com.

This work was supported by the Bundesministerium fuer Bildung und Forschung through the Deutsches Zentrum fuer Luft- und Raumfahrt, Germany, (grant number 01KI2077) and by the Federal State of Baden-Wuerttemberg, Germany, MWK-Sonderfoerdermaßnahme COVID-19/AZ.:33-7533.-6-21/7/2 to M. Schwemmle, Deutsche Forschungsgemeinschaft (DFG) to M. Beer (#453012513) and M. Schwemmle (SFB1160), and by the Swiss National Science Foundation as a part of NCCR RNA&-Disease, a National Centre of Competence (or Excellence) in Research (grant number 182880), and DFG (SPP1596) to V. Thiel. The work of S. Crotta, M. Llorian, and A. Wack was funded by the Francis Crick Institute, which receives its core funding from Cancer Research UK (FC001206), the UK Medical Research Council (FC001206), and the Wellcome Trust (FC001206). For the purpose of Open Access, the author has applied a CC BY public copyright licence to any Author Accepted Manuscript version arising from this submission. The funders had no role in the study design, data analysis, data interpretation, and in the writing of this report. All authors had full access to the data in the study and accept responsibility to submit for publication.

Author contributions: J. Beer and D. Schnepf designed and performed most of the experiments, analyzed and interpreted the data, and performed statistical analyses. S. Crotta and A. Breithaupt performed experiments, analyzed and interpreted the data, and performed statistical analyses. A. Ohnemus, J. Becker, B. Sachs, and L. Kern performed experiments and

processed and analyzed samples. M. Llorian analyzed, interpreted, and visualized data, and performed statistical analyses. L. Kern and J. Fuchs performed virus genome sequencing, analyzed, interpreted, and visualized data. N. Ebert, F. Labroussaa, T.T. Nhu Thao, B.S. Trueeb, J. Jores, V. Thiel, G. Kochs, and M. Beer generated and provided essential materials. M. Beer, G. Kochs, A. Wack, and M. Schwemmle interpreted data and gave advice. D. Schnepf and M. Schwemmle conceived the project. D. Schnepf wrote the manuscript with input from all authors.

Disclosures: The authors declare no competing interests exist.

Submitted: 8 April 2022
Revised: 5 August 2022
Accepted: 1 September 2022

References

Akamatsu, M.A., J.T. De Castro, C.Y. Takano, and P.L. Ho. 2021. Off balance: Interferons in COVID-19 lung infections. *EBioMedicine*. 73:103642. https://doi.org/10.1016/j.ebiom.2021.103642

Andersen, H., J. Meyer, J. Freeman, S.E. Doyle, K. Klucher, D.M. Miller, D. Hausman, and J.L. Hillson. 2013. Peginterferon lambda-1a, a new therapeutic for hepatitis C infection, from bench to clinic. *J. Clin. Transl. Hepatol.* 1:116–124. https://doi.org/10.14218/JCTH.2013.00014

Bartleson, J.M., D. Radenkovic, A.J. Covarrubias, D. Furman, D.A. Winer, and E. Verdin. 2021. SARS-CoV-2, COVID-19 and the ageing immune system. *Nat. Aging*. 1:769–782. https://doi.org/10.1038/s43587-021-00114-7

Bastard, P., A. Gervais, T. Le Voyer, J. Rosain, Q. Philippot, J. Manry, E. Michailidis, H.H. Hoffmann, S. Eto, M. Garcia-Prat, et al. 2021. Autoantibodies neutralizing type I IFNs are present in ∼4% of uninfected individuals over 70 years old and account for ∼20% of COVID-19 deaths. *Sci. Immunol.* 6:eabl4340. https://doi.org/10.1126/sciimmunol.abl4340

Bastard, P., L.B. Rosen, Q. Zhang, E. Michailidis, H.H. Hoffmann, Y. Zhang, K. Dorgham, Q. Philippot, J. Rosain, V. Béziat, et al. 2020. Autoantibodies against type I IFNs in patients with life-threatening COVID-19. *Science*. 370:eabd4585. https://doi.org/10.1126/science.abd4585

Bennett, A.J., A.C. Paskey, A. Ebinger, F. Pfaff, G. Priemer, D. Höper, A. Breithaupt, E. Heuser, R.G. Ulrich, J.H. Kuhn, et al. 2020. Relatives of rubella virus in diverse mammals. *Nature*. 586:424–428. https://doi.org/10.1038/s41586-020-2812-9

Broggi, A., S. Ghosh, B. Sposito, R. Spreafico, F. Balzarini, A. Lo Cascio, N. Clementi, M. De Santis, N. Mancini, F. Granucci, and I. Zanoni. 2020. Type III interferons disrupt the lung epithelial barrier upon viral recognition. *Science*. 369:706–712. https://doi.org/10.1126/science.abc3545

Busnadiego, I., S. Fernbach, M.O. Pohl, U. Karakus, M. Huber, A. Trkola, S. Stertz and B.G. Hale 2020. Antiviral activity of type I, II, and III interferons counterbalances ACE2 inducibility and restricts SARS-CoV-2. *mBio*. 11:e01928-20. https://doi.org/10.1128/mBio.01928-20

Caramaschi, S., M.E. Kapp, S.E. Miller, R. Eisenberg, J. Johnson, G. Epperly, A. Maiorana, G. Silvestri, and G.A. Giannico. 2021. Histopathological findings and clinicopathologic correlation in COVID-19: A systematic review. *Mod. Pathol.* 34:1614–1633. https://doi.org/10.1038/s41379-021-00814-w

Channappanavar, R., and S. Perlman. 2020. Age-related susceptibility to coronavirus infections: Role of impaired and dysregulated host immunity. *J. Clin. Invest.* 130:6204–6213. https://doi.org/10.1172/JCI144115

Chen, S., Y. Zhou, Y. Chen, and J. Gu. 2018. fastp: An ultra-fast all-in-one FASTQ preprocessor. *Bioinformatics*. 34:i884–i890. https://doi.org/10.1093/bioinformatics/bty560

Cingolani, P., A. Platts, L. Wang le, M. Coon, T. Nguyen, L. Wang, S.J. Land, X. Lu, and D.M. Ruden. 2012. A program for annotating and predicting the effects of single nucleotide polymorphisms, SnpEff: SNPs in the genome of Drosophila melanogaster strain w1118; iso-2; iso-3. *Fly*. 6:80–92. https://doi.org/10.4161/fly.19695

Corman, V.M., O. Landt, M. Kaiser, R. Molenkamp, A. Meijer, D.K. Chu, T. Bleicker, S. Brünink, J. Schneider, M.L. Schmidt, et al. 2020. Detection of 2019 novel coronavirus (2019-nCoV) by real-time RT-PCR. *Euro Surveill.* 25:2000045. https://doi.org/10.2807/1560-7917.es.2020.25.3.2000045

Couper, K.N., D.G. Blount, and E.M. Riley. 2008. IL-10: The master regulator of immunity to infection. *J. Immunol.* 180:5771–5777. https://doi.org/10.4049/jimmunol.180.9.5771

Davidson, S., T.M. Mccabe, S. Crotta, H.H. Gad, E.M. Hessel, S. Beinke, R. Hartmann, and A. Wack. 2016. IFNλ is a potent anti-influenza therapeutic without the inflammatory side effects of IFNα treatment. *EMBO Mol. Med.* 8:1099–1112. https://doi.org/10.15252/emmm.201606413

Di Tommaso, P., M. Chatzou, E.W. Floden, P.P. Barja, E. Palumbo, and C. Notredame. 2017. Nextflow enables reproducible computational workflows. *Nat. Biotechnol.* 35:316–319. https://doi.org/10.1038/nbt.3820

Dinnon, K.H., S.R. Leist, A. Schäfer, C.E. Edwards, D.R. Martinez, S.A. Montgomery, A. West, B.L. Yount, Y.J. Hou, L.E. Adams, et al. 2020. A mouse-adapted model of SARS-CoV-2 to test COVID-19 countermeasures. *Nature*. 586:560–566. https://doi.org/10.1038/s41586-020-2708-8

Dobin, A., C.A. Davis, F. Schlesinger, J. Drenkow, C. Zaleski, S. Jha, P. Batut, M. Chaisson, and T.R. Gingeras. 2013. STAR: Ultrafast universal RNA-seq aligner. *Bioinformatics*. 29:15–21. https://doi.org/10.1093/bioinformatics/bts635

Ewels, P.A., A. Peltzer, S. Fillinger, H. Patel, J. Alneberg, A. Wilm, M.U. Garcia, P. Di Tommaso, and S. Nahnsen. 2020. The nf-core framework for community-curated bioinformatics pipelines. *Nat. Biotechnol.* 38:276–278. https://doi.org/10.1038/s41587-020-0439-x

Feld, J.J., C. Kandel, M.J. Biondi, R.A. Kozak, M.A. Zahoor, C. Lemieux, S.M. Borgia, A.K. Boggild, J. Powis, J. Mccready, et al. 2021. Peginterferon lambda for the treatment of outpatients with COVID-19: A phase 2, placebo-controlled randomised trial. *Lancet Respir. Med.* 9:498–510. https://doi.org/10.1016/S2213-2600(20)30566-X

Fenimore, J., and H.A. Young. 2016. Regulation of IFN-γ Expression. *In* Regulation of Cytokine Gene Expression in Immunity and Diseases. X. Ma, editor. Springer Netherlands, Dordrecht.

Galani, I.-E., N. Rovina, V. Lampropoulou, V. Triantafyllia, M. Manioudaki, E. Pavlos, E. Koukaki, P.C. Fragkou, V. Panou, V. Rapti, et al. 2021. Untuned antiviral immunity in COVID-19 revealed by temporal type I/III interferon patterns and flu comparison. *Nat. Immunol.* 22:32–40. https://doi.org/10.1038/s41590-020-00840-x

Galani, I.E., V. Triantafyllia, E.E. Eleminiadou, O. Koltsida, A. Stavropoulos, M. Manioudaki, D. Thanos, S.E. Doyle, S.V. Kotenko, K. Thanopoulou, and E. Andreakos. 2017. Interferon-λ mediates non-redundant front-line antiviral protection against influenza virus infection without compromising host fitness. *Immunity*. 46:875–890.e6. https://doi.org/10.1016/j.immuni.2017.04.025

Gawish, R., P. Starkl, L. Pimenov, A. Hladik, K. Lakovits, F. Oberndorfer, S.J. Cronin, A. Ohradanova-Repic, G. Wirnsberger, B. Agerer, et al. 2022. ACE2 is the critical in vivo receptor for SARS-CoV-2 in a novel COVID-19 mouse model with TNF- and IFNγ-driven immunopathology. *Elife*. 11:e74623. https://doi.org/10.7554/eLife.74623

Gu, H., Q. Chen, G. Yang, L. He, H. Fan, Y.Q. Deng, Y. Wang, Y. Teng, Z. Zhao, Y. Cui, et al. 2020. Adaptation of SARS-CoV-2 in BALB/c mice for testing vaccine efficacy. *Science*. 369:1603–1607. https://doi.org/10.1126/science.abc4730

Hadjadj, J., N. Yatim, L. Barnabei, A. Corneau, J. Boussier, N. Smith, H. Péré, B. Charbit, V. Bondet, C. Chenevier-Gobeaux, et al. 2020. Impaired type I interferon activity and inflammatory responses in severe COVID-19 patients. *Science*. 369:718–724. https://doi.org/10.1126/science.abc6027

Heuberger, J., J. Trimpert, D. Vladimirova, C. Goosmann, M. Lin, R. Schmuck, H.J. Mollenkopf, V. Brinkmann, F. Tacke, N. Osterrieder, and M. Sigal. 2021. Epithelial response to IFN-γ promotes SARS-CoV-2 infection. *EMBO Mol. Med.* 13:e13191. https://doi.org/10.15252/emmm.202013191

Horisberger, M.A., and K. De Staritzky. 1987. A recombinant human interferon-alpha B/D hybrid with a broad host-range. *J. Gen. Virol.* 68:945–948. https://doi.org/10.1099/0022-1317-68-3-945

Jagannathan, P., J.R. Andrews, H. Bonilla, H. Hedlin, K.B. Jacobson, V. Balasubramanian, N. Purington, S. Kamble, C.R. De Vries, O. Quintero, et al. 2021. Peginterferon lambda-1a for treatment of outpatients with uncomplicated COVID-19: A randomized placebo-controlled trial. *Nat. Commun.* 12:1967. https://doi.org/10.1038/s41467-021-22177-1

Kaleta, T., L. Kern, S.L. Hong, M. Hölzer, G. Kochs, J. Beer, D. Schnepf, M. Schwemmle, N. Bollen, P. Kolb, et al. 2022. Antibody Escape and Global Spread of SARS-CoV-2 Lineage A.27. *Nat Commun.* 13:1152. https://doi.org/10.1038/s41467-022-28766-y

Karki, R., and T.D. Kanneganti. 2021. The "cytokine storm": Molecular mechanisms and therapeutic prospects. *Trends Immunol.* 42:681–705. https://doi.org/10.1016/j.it.2021.06.001

Karki, R., B.R. Sharma, S. Tuladhar, E.P. Williams, L. Zalduondo, P. Samir, M. Zheng, B. Sundaram, B. Banoth, R.K.S. Malireddi, et al. 2021. Synergism of TNF-α and IFN-γ triggers inflammatory cell death, tissue damage, and mortality in SARS-CoV-2 infection and cytokine shock syndromes. *Cell*. 184:149–168.e17. https://doi.org/10.1016/j.cell.2020.11.025

Klinkhammer, J., D. Schnepf, L. Ye, M. Schwaderlapp, H.H. Gad, R. Hartmann, D. Garcin, T. Mahlakoiv, and P. Staeheli. 2018. IFN-lambda prevents influenza virus spread from the upper airways to the lungs and limits virus transmission. *Elife*. 7:e33354. https://doi.org/10.7554/eLife.33354

Krämer, B., R. Knoll, L. Bonaguro, M. Tovinh, J. Raabe, R. Astaburuaga-García, J. Schulte-Schrepping, K.M. Kaiser, G.J. Rieke, J. Bischoff, et al. 2021. Early IFN-α signatures and persistent dysfunction are distinguishing features of NK cells in severe COVID-19. *Immunity*. 54:2650–2669.e14. https://doi.org/10.1016/j.immuni.2021.09.002

Kumar, A.B., A.H., and B. Gruening. 2020. Community research amid COVID-19 Pandemic: Genomics analysis of SARS-CoV-2 over Public GALAXY Server. *Preprints*. https://doi.org/10.20944/preprints202005.0343.v1

Kurtzer, G.M., V. Sochat, and M.W. Bauer. 2017. Singularity: Scientific containers for mobility of compute. *PLoS One*. 12:e0177459. https://doi.org/10.1371/journal.pone.0177459

Leist, S.R., K.H. Dinnon, A. Schäfer, L.V. Tse, K. Okuda, Y.J. Hou, A. West, C.E. Edwards, W. Sanders, E.J. Fritch, et al. 2020. A mouse-adapted SARS-CoV-2 induces acute lung injury and mortality in standard laboratory mice. *Cell*. 183:1070–1085.e12. https://doi.org/10.1016/j.cell.2020.09.050

Li, B., and C.N. Dewey. 2011. RSEM: Accurate transcript quantification from RNA-seq data with or without a reference genome. *BMC Bioinf.* 12:323. https://doi.org/10.1186/1471-2105-12-323

Li, H., and R. Durbin. 2009. Fast and accurate short read alignment with Burrows-Wheeler transform. *Bioinformatics*. 25:1754–1760. https://doi.org/10.1093/bioinformatics/btp324

Li, H., B. Handsaker, A. Wysoker, T. Fennell, J. Ruan, N. Homer, G. Marth, G. Abecasis, R. Durbin, and 1000 Genome Project Data Processing Subgroup. 2009. The sequence alignment/map format and SAMtools. *Bioinformatics*. 25:2078–2079. https://doi.org/10.1093/bioinformatics/btp352

Loske, J., J. Röhmel, S. Lukassen, S. Stricker, V.G. Magalhães, J. Liebig, R.L. Chua, L. Thürmann, M. Messingschlager, A. Seegebarth, et al. 2021. Pre-activated antiviral innate immunity in the upper airways controls early SARS-CoV-2 infection in children. *Nat. Biotechnol.* 40:319–324. https://doi.org/10.1038/s41587-021-01037-9

Love, M.I., W. Huber, and S. Anders. 2014. Moderated estimation of fold change and dispersion for RNA-seq data with DESeq2. *Genome Biol.* 15:550. https://doi.org/10.1186/s13059-014-0550-8

Lucas, C., P. Wong, J. Klein, T.B.R. Castro, J. Silva, M. Sundaram, M.K. Ellingson, T. Mao, J.E. Oh, B. Israelow, et al. 2020. Longitudinal analyses reveal immunological misfiring in severe COVID-19. *Nature*. 584:463–469. https://doi.org/10.1038/s41586-020-2588-y

Major, J., S. Crotta, M. Llorian, T.M. Mccabe, H.H. Gad, S.L. Priestnall, R. Hartmann, and A. Wack. 2020. Type I and III interferons disrupt lung epithelial repair during recovery from viral infection. *Science*. 369:712–717. https://doi.org/10.1126/science.abc2061

Meisel, C., B. Akbil, T. Meyer, E. Lankes, V.M. Corman, O. Staudacher, N. Unterwalder, U. Kölsch, C. Drosten, M.A. Mall, et al. 2021. Mild COVID-19 despite autoantibodies against type I IFNs in autoimmune polyendocrine syndrome type 1. *J. Clin. Invest.* 131:e150867. https://doi.org/10.1172/JCI150867

Meyerholz, D.K., and A.P. Beck. 2018. Principles and approaches for reproducible scoring of tissue stains in research. *Lab. Invest.* 98:844–855. https://doi.org/10.1038/s41374-018-0057-0

Montagutelli, X., M. Prot, L. Levillayer, E.B. Salazar, G. Jouvion, L. Conquet, M. Beretta, F. Donati, M. Albert, F. Gambaro, et al. 2021. Variants with the N501Y mutation extend SARS-CoV-2 host range to mice, with contact transmission. *bioRxiv*. (Preprint Posted December 07, 2021). https://doi.org/10.1101/2021.03.18.436013

Muir, A.J., M.L. Shiffman, A. Zaman, B. Yoffe, A. De La Torre, S. Flamm, S.C. Gordon, P. Marotta, J.M. Vierling, J.C. Lopez-Talavera, et al. 2010. Phase 1b study of pegylated interferon lambda 1 with or without ribavirin in patients with chronic genotype 1 hepatitis C virus infection. *Hepatology*. 52:822–832. https://doi.org/10.1002/hep.23743

Muruato, A., M.N. Vu, B.A. Johnson, M.E. Davis-Gardner, A. Vanderheiden, K. Lokugamage, C. Schindewolf, P.A. Crocquet-Valdes, R.M. Langsjoen, J.A. Plante, et al. 2021. Mouse-adapted SARS-CoV-2 protects animals from lethal SARS-CoV challenge. *PLoS Biol.* 19:e3001284. https://doi.org/10.1371/journal.pbio.3001284

Nelson, M., R. Rubio, A. Lazzarin, S. Romanova, A. Luetkemeyer, B. Conway, J.M. Molina, D. Xu, S. Srinivasan, and S. Portsmouth. 2017. Safety and efficacy of pegylated interferon lambda, ribavirin, and daclatasvir in HCV and HIV-coinfected patients. *J. Interferon Cytokine Res.* 37:103–111. https://doi.org/10.1089/jir.2016.0082

O'driscoll, M., G. Ribeiro Dos Santos, L. Wang, D.A.T. Cummings, A.S. Azman, J. Paireau, A. Fontanet, S. Cauchemez, and H. Salje. 2021. Age-specific mortality and immunity patterns of SARS-CoV-2. *Nature*. 590:140–145. https://doi.org/10.1038/s41586-020-2918-0

Paludan, S.R., and T.H. Mogensen. 2022. Innate immunological pathways in COVID-19 pathogenesis. *Sci. Immunol.* 7:eabm5505. https://doi.org/10.1126/sciimmunol.abm5505

Pannone, G., V.C.A. Caponio, I.S. De Stefano, M.A. Ramunno, M. Meccariello, A. Agostinone, M.C. Pedicillo, G. Troiano, K. Zhurakivska, T. Cassano, et al. 2021. Lung histopathological findings in COVID-19 disease – a systematic review. *Infect. Agents Cancer*. 16:34. https://doi.org/10.1186/s13027-021-00369-0

Park, A., and A. Iwasaki. 2020. Type I and type III interferons – induction, signaling, evasion, and application to combat COVID-19. *Cell Host Microbe*. 27:870–878. https://doi.org/10.1016/j.chom.2020.05.008

Pekayvaz, K., A. Leunig, R. Kaiser, M. Joppich, S. Brambs, A. Janjic, O. Popp, D. Nixdorf, V. Fumagalli, N. Schmidt, et al. 2022. Protective immune trajectories in early viral containment of non-pneumonic SARS-CoV-2 infection. *Nat. Commun.* 13:1018. https://doi.org/10.1038/s41467-022-28508-0

Rathnasinghe, R., S. Jangra, A. Cupic, C. Martínez-Romero, L.C.F. Mulder, T. Kehrer, S. Yildiz, A. Choi, I. Mena, J. De Vrieze, et al. 2021. The N501Y Mutation in SARS-CoV-2 Spike Leads to Morbidity in Obese and Aged Mice and Is Neutralized by Convalescent and Post-vaccination Human Sera. *medRxiv*. (Preprint posted January 20, 2021). https://doi.org/10.1101/2021.01.19.21249592

Schepens, B., L. Van Schie, W. Nerinckx, K. Roose, W. Van Breedam, D. Fijalkowska, S. Devos, W. Weyts, S. De Cae, S. Vanmarcke, et al. 2021. An affinity-enhanced, broadly neutralizing heavy chain-only antibody protects against SARS-CoV-2 infection in animal models. *Sci. Transl. Med.* 13:eabi7826. https://doi.org/10.1126/scitranslmed.abi7826

Schlottau, K., M. Rissmann, A. Graaf, J. Schön, J. Sehl, C. Wylezich, D. Höper, T.C. Mettenleiter, A. Balkema-Buschmann, T. Harder, et al. 2020. SARS-CoV-2 in fruit bats, ferrets, pigs, and chickens: An experimental transmission study. *Lancet Microbe*. 1:e218–e225. https://doi.org/10.1016/S2666-5247(20)30089-6

Schnepf, D., S. Crotta, T. Thamamongood, M. Stanifer, L. Polcik, A. Ohnemus, J. Vier, C. Jakob, M. Llorian, H.H. Gad, et al. 2021. Selective Janus kinase inhibition preserves interferon-lambda-mediated antiviral responses. *Sci. Immunol.* 6:eabd5318. https://doi.org/10.1126/sciimmunol.abd5318

Shaw, A.C., D.R. Goldstein, and R.R. Montgomery. 2013. Age-dependent dysregulation of innate immunity. *Nat. Rev. Immunol.* 13:875–887. https://doi.org/10.1038/nri3547

Shuai, H., J.F.-W. Chan, T.T.-T. Yuen, C. Yoon, J.-C. Hu, L. Wen, B. Hu, D. Yang, Y. Wang, Y. Hou, et al. 2021. Emerging SARS-CoV-2 variants expand species tropism to murines. *EBioMedicine*. 73:103643. https://doi.org/10.1016/j.ebiom.2021.103643

Smaldone, G.C. 2018. Repurposing of gamma interferon via inhalation delivery. *Adv. Drug Deliv. Rev.* 133:87–92. https://doi.org/10.1016/j.addr.2018.06.004

Sodeifian, F., M. Nikfarjam, N. Kian, K. Mohamed, and N. Rezaei. 2022. The role of type I interferon in the treatment of COVID-19. *J. Med. Virol.* 94:63–81. https://doi.org/10.1002/jmv.27317

Sposito, B., A. Broggi, L. Pandolfi, S. Crotta, N. Clementi, R. Ferrarese, S. Sisti, E. Criscuolo, R. Spreafico, J.M. Long, et al. 2021. The interferon landscape along the respiratory tract impacts the severity of COVID-19. *Cell*. 184:4953–4968.e16. https://doi.org/10.1016/j.cell.2021.08.016

Sun, S.H., Q. Chen, H.J. Gu, G. Yang, Y.X. Wang, X.Y. Huang, S.S. Liu, N.N. Zhang, X.F. Li, R. Xiong, et al. 2020. A mouse model of SARS-CoV-2 infection and pathogenesis. *Cell Host Microbe*. 28:124–133.e4. https://doi.org/10.1016/j.chom.2020.05.020

Thi Nhu Thao, T., F. Labroussaa, N. Ebert, P. V'kovski, H. Stalder, J. Portmann, J. Kelly, S. Steiner, M. Holwerda, A. Kratzel, et al. 2020. Rapid reconstruction of SARS-CoV-2 using a synthetic genomics platform. *Nature*. 582:561–565. https://doi.org/10.1038/s41586-020-2294-9

Todd, P.A., and K.L. Goa. 1992. Interferon gamma-1b. A review of its pharmacology and therapeutic potential in chronic granulomatous disease. *Drugs*. 43:111–122. https://doi.org/10.2165/00003495-199243010-00008

Trinchieri, G. 2007. Interleukin-10 production by effector T cells: Th1 cells show self control. *J. Exp. Med.* 204:239–243. https://doi.org/10.1084/jem.20070104

Vijay, R., X. Hua, D.K. Meyerholz, Y. Miki, K. Yamamoto, M. Gelb, M. Murakami, and S. Perlman. 2015. Critical role of phospholipase A2 group IID in age-related susceptibility to severe acute respiratory syndrome-CoV infection. *J. Exp. Med.* 212:1851–1868. https://doi.org/10.1084/jem.20150632

Wagner, T.R., D. Schnepf, J. Beer, N. Ruetalo, K. Klingel, P.D. Kaiser, D. Junker, M. Sauter, B. Traenkle, D.I. Frecot, et al. 2021. Biparatopic nanobodies protect mice from lethal challenge with SARS-CoV-2 variants of concern. *EMBO Rep.* 23:e53865. https://doi.org/10.15252/embr.202153865

Wang, E.Y., T. Mao, J. Klein, Y. Dai, J.D. Huck, J.R. Jaycox, F. Liu, T. Zhou, B. Israelow, P. Wong, et al. 2021. Diverse functional autoantibodies in patients with covid-19. *Nature.* 595:283–288. https://doi.org/10.1038/s41586-021-03631-y

Wang, N., Y. Zhan, L. Zhu, Z. Hou, F. Liu, P. Song, F. Qiu, X. Wang, X. Zou, D. Wan, et al. 2020. Retrospective multicenter cohort study shows early interferon therapy is associated with favorable clinical responses in COVID-19 patients. *Cell Host Microbe.* 28:455–464.e2. https://doi.org/10.1016/j.chom.2020.07.005

Werder, R.B., J.P. Lynch, J.C. Simpson, V. Zhang, N.H. Hodge, M. Poh, E. Forbes-Blom, C. Kulis, M.L. Smythe, J.W. Upham, et al. 2018. PGD2/DP2 receptor activation promotes severe viral bronchiolitis by suppressing IFN-λ production. *Sci. Transl. Med.* 10:eaao0052. https://doi.org/10.1126/scitranslmed.aao0052

WHO. 2022. WHO coronavirus (COVID-19) dashboard [online]. Available: https://covid19.who.int/ [Accessed 01.08.2022 2022]

Wilm, A., P.P. Aw, D. Bertrand, G.H. Yeo, S.H. Ong, C.H. Wong, C.C. Khor, R. Petric, M.L. Hibberd, and N. Nagarajan. 2012. LoFreq: A sequence-quality aware, ultra-sensitive variant caller for uncovering cell-population heterogeneity from high-throughput sequencing datasets. *Nucleic Acids Res.* 40:11189–11201. https://doi.org/10.1093/nar/gks918

Winkler, E.S., A.L. Bailey, N.M. Kafai, S. Nair, B.T. Mccune, J. Yu, J.M. Fox, R.E. Chen, J.T. Earnest, S.P. Keeler, et al. 2020. SARS-CoV-2 infection of human ACE2-transgenic mice causes severe lung inflammation and impaired function. *Nat. Immunol.* 21:1327–1335. https://doi.org/10.1038/s41590-020-0778-2

Winkler, E.S., R.E. Chen, F. Alam, S. Yildiz, J.B. Case, M.B. Uccellini, M.J. Holtzman, A. Garcia-Sastre, M. Schotsaert, M.S. Diamond, and S. Schultz-Cherry. 2022. SARS-CoV-2 causes lung infection without severe disease in human ACE2 knock-in mice. *J. Virol.* 96:e0151121. https://doi.org/10.1128/JVI.01511-21

Witkowski, M., C. Tizian, M. Ferreira-Gomes, D. Niemeyer, T.C. Jones, F. Heinrich, S. Frischbutter, S. Angermair, T. Hohnstein, I. Mattiola, et al. 2021. Untimely TGFβ responses in COVID-19 limit antiviral functions of NK cells. *Nature.* 600:295–301. https://doi.org/10.1038/s41586-021-04142-6

Wong, L.-Y.R., and S. Perlman. 2022. Immune dysregulation and immunopathology induced by SARS-CoV-2 and related coronaviruses — are we our own worst enemy? *Nat. Rev. Immunol.* 22:47–56. https://doi.org/10.1038/s41577-021-00656-2

Wong, L.-Y.R., J. Zheng, K. Wilhelmsen, K. Li, M.E. Ortiz, N.J. Schnicker, A. Thurman, A.A. Pezzulo, P.J. Szachowicz, P. Li, et al. 2022. Eicosanoid signalling blockade protects middle-aged mice from severe COVID-19. *Nature.* 605:146–151. https://doi.org/10.1038/s41586-022-04630-3

Ye, L., D. Schnepf, J. Becker, K. Ebert, Y. Tanriver, V. Bernasconi, H.H. Gad, R. Hartmann, N. Lycke, and P. Staeheli. 2019a. Interferon-λ enhances adaptive mucosal immunity by boosting release of thymic stromal lymphopoietin. *Nat. Immunol.* 20:593–601. https://doi.org/10.1038/s41590-019-0345-x

Ye, L., D. Schnepf, and P. Staeheli. 2019b. Interferon-λ orchestrates innate and adaptive mucosal immune responses. *Nat. Rev. Immunol.* 19:614–625. https://doi.org/10.1038/s41577-019-0182-z

Yoshida, M., K.B. Worlock, N. Huang, R.G.H. Lindeboom, C.R. Butler, N. Kumasaka, C. Dominguez Conde, L. Mamanova, L. Bolt, L. Richardson, et al. 2022. Local and systemic responses to SARS-CoV-2 infection in children and adults. *Nature.* 602:321–327. https://doi.org/10.1038/s41586-021-04345-x

Yu, D., M. Zhao, L. Dong, L. Zhao, M. Zou, H. Sun, M. Zhang, H. Liu, and Z. Zou. 2016. Design and evaluation of novel interferon lambda analogs with enhanced antiviral activity and improved drug attributes. *Drug Des. Devel. Ther.* 10:163–182. https://doi.org/10.2147/DDDT.S91455

Zhang, Q., P. Bastard, Z. Liu, J. Le Pen, M. Moncada-Velez, J. Chen, M. Ogishi, I.K.D. Sabli, S. Hodeib, C. Korol, et al. 2020. Inborn errors of type I IFN immunity in patients with life-threatening COVID-19. *Science.* 370:eabd4570. https://doi.org/10.1126/science.abd4570

Zhao, J., J. Zhao, K. Legge, and S. Perlman. 2011. Age-related increases in PGD(2) expression impair respiratory DC migration, resulting in diminished T cell responses upon respiratory virus infection in mice. *J. Clin. Invest.* 121:4921–4930. https://doi.org/10.1172/JCI59777

Zhou, B., T.T.N. Thao, D. Hoffmann, A. Taddeo, N. Ebert, F. Labroussaa, A. Pohlmann, J. King, S. Steiner, J.N. Kelly, et al. 2021. SARS-CoV-2 spike D614G change enhances replication and transmission. *Nature.* 592:122–127. https://doi.org/10.1038/s41586-021-03361-1

Supplemental material

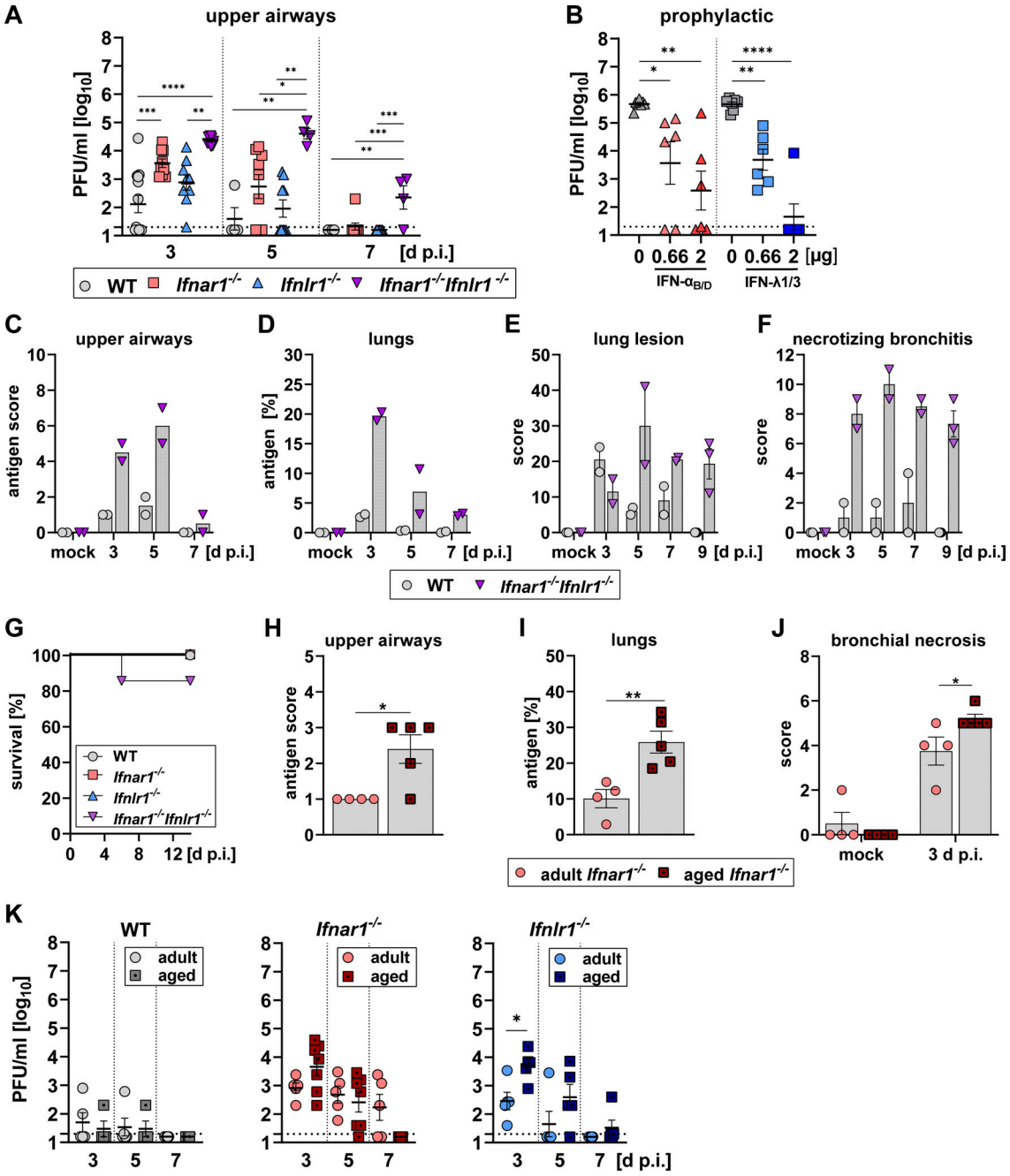

Figure S1. **Increased and prolonged replication of SARS-CoV-2 MA in mice lacking type I and/or type III IFN receptors. (A)** Groups of adult mice (8–18-wk-old) of the indicated genotypes were infected with 10^5 PFU SARS-CoV-2 MA. Upper airways were harvested at the indicated time points and viral load determined by plaque assay on Vero E6 cells. Data pooled from five independent experiments. Symbols represent individual mice (n = 4–13 per group) and bars indicate mean ± SEM. Dashed line indicates detection limit. *P ≤ 0.05, **P ≤ 0.01, ***P ≤ 0.001, ****P ≤ 0.0001, one-way ANOVA with Tukey's multiple comparisons test. **(B)** Groups of 16–24 wk-old *Ifnlr1*$^{-/-}$ (triangles) and *Ifnar1*$^{-/-}$ mice (squares) were intranasally treated with the indicated dose of IFN-$\alpha_{B/D}$ or IFN-λ1/3, respectively, or mock-treated 1 d prior to infection with 10^5 PFU SARS-CoV-2 MA. Lung viral loads on day 3 p.i. were determined by plaque assay on Vero E6 cells. Data from a single experiment are shown. Symbols represent individual mice (n = 6–7 per group) and bars indicate mean ± SEM. Dashed line indicates detection limit. *P ≤ 0.05, **P ≤ 0.01, ****P ≤ 0.0001, one-way ANOVA with Tukey's multiple comparisons test. **(C–F)** Groups of adult (8–10-wk-old) WT or *Ifnar1*$^{-/-}$ *Ifnlr1*$^{-/-}$ mice were mock-treated or infected with 10^5 PFU SARS-CoV-2 MA (n = 2–3 per group) and prepared for histological analyses by cardiac perfusion. Antigen and histopathologic lesion scores for lungs and necrotizing bronchitis were quantified as described in Materials and methods section. Data pooled from two independent experiments are shown. Symbols represent individual mice and bars indicate mean ± SEM. **(G)** Survival graph corresponding to Fig. 1 D. **(H–J)** Groups of adult (8–10-wk-old; n = 4) or aged *Ifnar1*$^{-/-}$ mice (36–52-wk-old; n = 5) were infected with 10^5 PFU SARS-CoV-2 MA. Mice were prepared for histological analyses by cardiac perfusion on day 3 p.i. Antigen and histopathologic lesion scores for bronchial necrosis were quantified as described in Materials and methods section. *P ≤ 0.05, **P ≤ 0.01, unpaired t test. **(K)** Groups of adult or aged mice (8–12-wk- or 40–60-wk-old; n = 4–7) of the indicated genotypes were infected with 10^5 PFU SARS-CoV-2 MA. Upper airways were harvested at the indicated time points and viral loads determined by plaque assay on Vero E6 cells. Data pooled from four independent experiments are shown. Symbols represent individual mice and bars indicate mean ± SEM. Dashed line indicates detection limit. *P ≤ 0.05, unpaired t test.

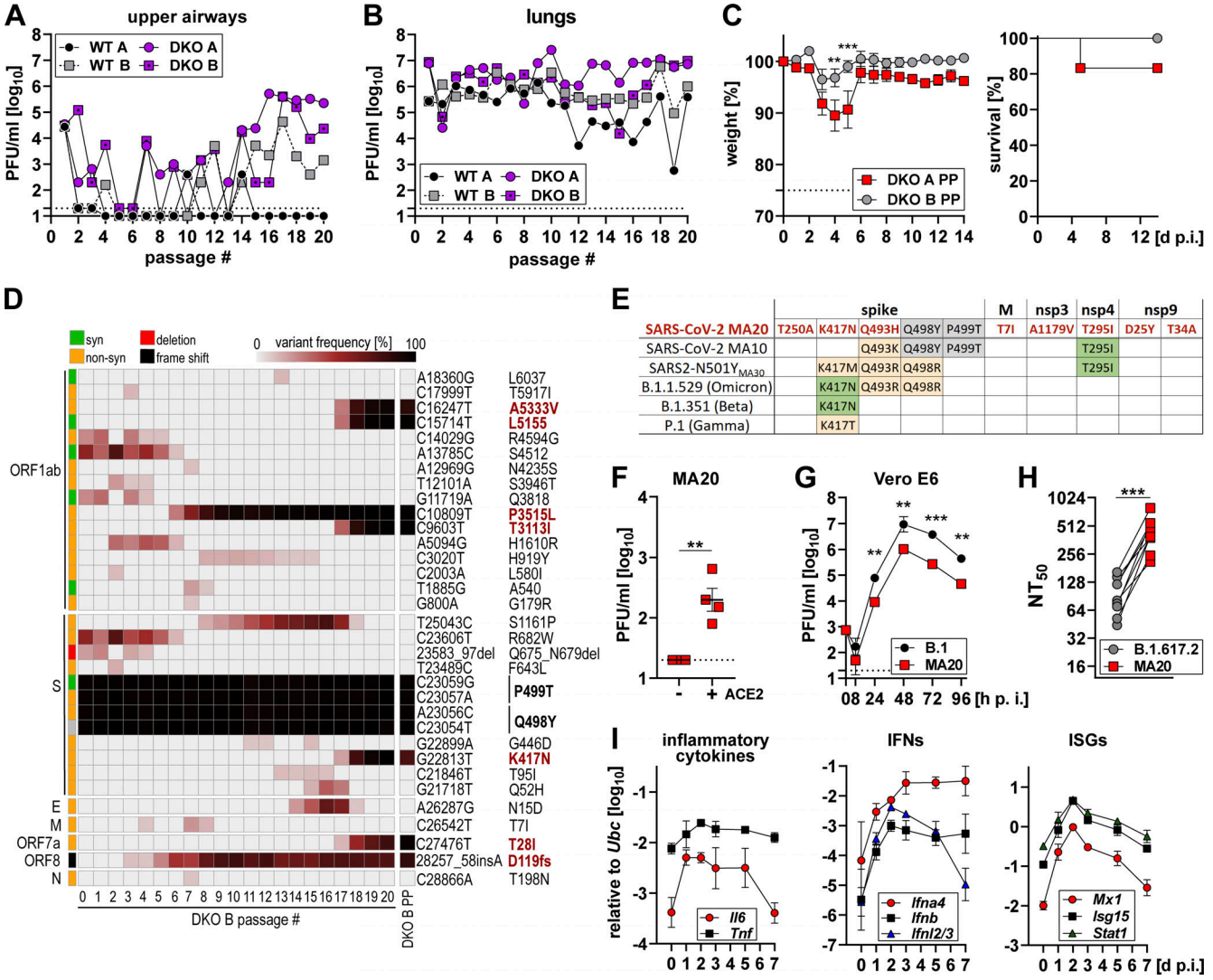

Figure S2. **Serial passaging of MA SARS-CoV-2 in IFN receptor-deficient C57BL/6 mice allows for rapid host adaptation. (A and B)** Viral load on day 3 p.i. in upper airways (A) and lungs (B) for passaging series WT A, WT B, DKO A, and DKO B determined by plaque assay on Vero E6 cells. Dashed line indicates detection limit. **(C)** Weight loss (left panel) and survival (right panel) of adult C57BL/6 WT mice (13–15-wk-old; n = 6 per group) infected with 5×10^3 PFU of PP virus stocks DKO A PP and DKO B PP. Data from a single experiment are shown. Symbols represent individual mice and bars indicate mean ± SEM. Dashed line indicates experimental endpoint due to animal welfare. **P ≤ 0.01, ***P ≤ 0.001, two-way ANOVA with Šídák's multiple comparisons test. **(D)** Variant frequency plot from next-generation sequencing results for the passaging series DKO B and the PP DKO B PP virus stock. Variant frequencies are shown in comparison to Wuhan-Hu-1 (NC_045512.2). Amino acid changes present in DKO B PP are indicated in bold, changes in comparison to SARS-CoV-2 MA are highlighted in red. Syn = synonymous; non-syn = non-synonymous. **(E)** Table indicating similar (orange) or identical (green) amino acid changes present in MA10, SARS2-N501$_{MA30}$, B1-1-529 (Omicron), B.1.351 (Beta), and P.1 (Gamma) in comparison with amino acid changes present in MA20 (red). Reference sequence: Wuhan-Hu-1 (NC_045512.2). Amino acid changes highlighted in gray were already present in SARS-CoV-2 MA. **(F)** ACE2 dependent entry of MA20 was evaluated by infecting ACE2 expressing A549 cells with an MOI of 0.1 in comparison with control A549 cells. Virus replication 4 d p.i. was quantified by plaque assay on Vero E6 cells. Data from a single experiment are shown. Symbols represent technical replicates and bars indicate mean ± SEM. Dashed line indicates detection limit. **P ≤ 0.01, unpaired t test. **(G)** Comparative growth curves of B.1 and MA20 on VeroE6 cells infected with an MOI of 0.001. Virus replication was quantified by plaque assay on Vero E6 cells. Data from a single experiment performed in duplicates are shown. Dashed line indicates detection limit. **P ≤ 0.01, ***P ≤ 0.001, two-way ANOVA with Tukey's multiple comparisons test. **(H)** Comparative neutralization by plaque reduction neutralization test of MA20 and B.1.617.2 (Delta) using sera from vaccinated individuals. Symbols represent mean value for each individual determined in three independent assays. ***P ≤ 0.001, paired t test. **(I)** Adult C57BL/6 mice (10-wk-old; n = 5 per group) were infected with 10^3 PFU of MA20. Upper airways were harvested at the indicated time points and gene expression levels of *Il6*, *Tnf*, *Ifna4*, *Ifnb*, *Ifnl2/3*, *Mx1*, *Isg15*, and *Stat1* were determined relative to *Ubc* by RT-qPCR. Symbols represent mean ± SD.

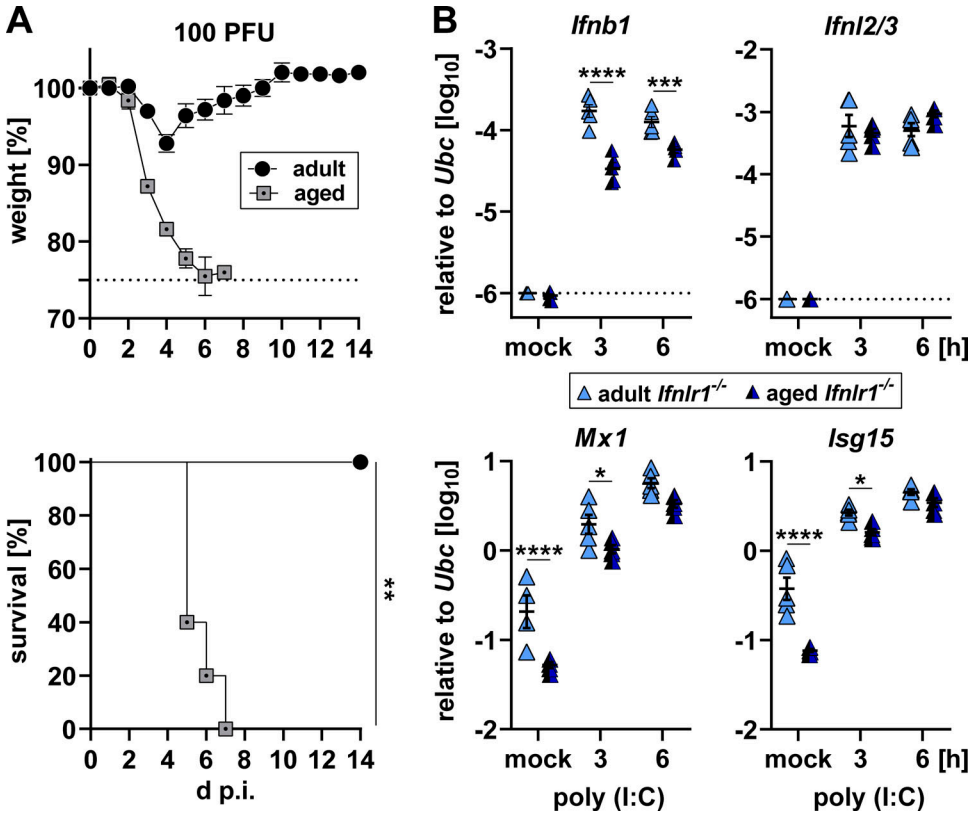

Figure S3. **Increased disease susceptibility of aged mice is associated with an impaired type I IFN response. (A)** Groups of adult or aged C57BL/6 (10-wk- or 40-wk-old; *n* = 5 per group) were infected with 100 PFU MA20. Weight loss (upper panel) and survival (lower panel) were monitored for 14 d p.i. Data from a single experiment are shown. Symbols represent mean ± SEM. Dashed line indicates experimental endpoint due to animal welfare. Survival: **P ≤ 0.01, Log-rank (Mantel-Cox) test. Dataset for infected 10-wk-old mice is also blotted in Fig. 2 G. **(B)** Groups of adult or aged *Ifnlr1*$^{-/-}$ mice (12-wk- or 52-wk-old; *n* = 5 per group) were mock-treated or intranasally inoculated with 40 µg of poly (I:C). Lungs were harvested at the indicated time points and gene expression levels of *Ifnb1*, *Ifnl2/3*, *Mx1*, and *Isg15* determined relative to *Ubc* by RT-qPCR. Data from a single experiment are shown. Symbols represent individual mice and bars indicate mean ± SEM. *P ≤ 0.05, ***P ≤ 0.001, ****P ≤ 0.0001, two-way ANOVA with Šídák's multiple comparisons test.

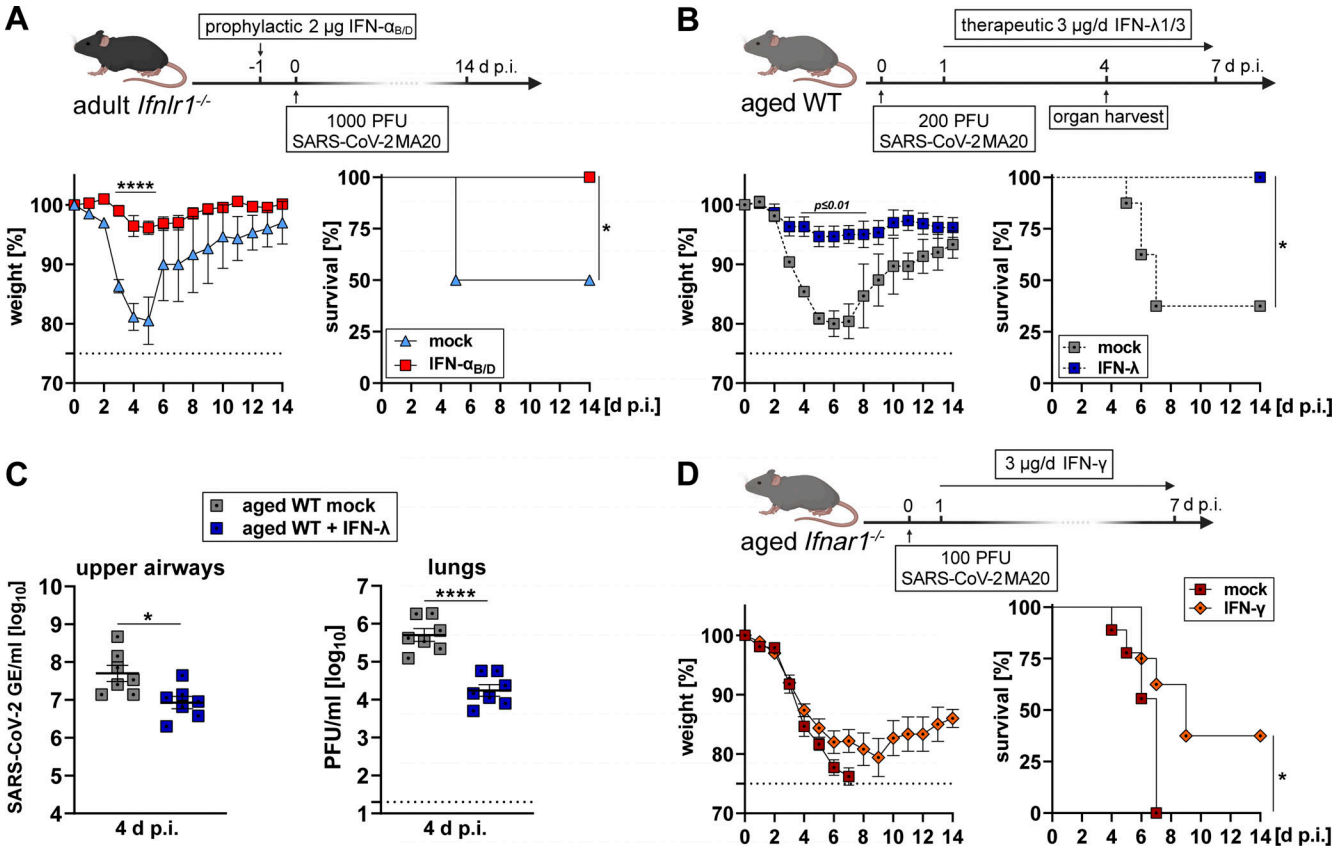

Figure S4. **Prophylactic IFN-α and therapeutic IFN-λ or IFN-γ treatment reduces SARS-CoV-2 induced lethality in highly susceptible mice. (A)** Groups of adult *Ifnlr1*$^{-/-}$ mice (13–15-wk-old) were either mock-treated (n = 6) or treated prophylactically by subcutaneous injection of 2 µg IFN-$\alpha_{B/D}$ once 1 d prior to infection (n = 7) with 1,000 PFU MA20. Dashed line indicates experimental endpoint due to animal welfare. Data from a single experiment are shown. Symbols represent mean ± SEM. Weight loss: ****P ≤ 0.0001, by two-way ANOVA with Šídák's multiple comparisons test. Survival: Log-rank (Mantel-Cox) test; *P ≤ 0.05. **(B)** Groups of aged WT mice (45–56-wk-old) were either mock-treated (n = 8) or treated therapeutically with 3 µg IFN-λ1/3 (n = 8) daily for 1 wk starting 1 d after infection with 200 PFU MA20. Mock-treated control group is the same as depicted in Fig. 7 C. Data from a single experiment are shown. Dashed line indicates experimental endpoint due to animal welfare. Symbols represent mean ± SEM. Weight loss: P ≤ 0.05 by two-way ANOVA with Šídák's multiple comparisons test. Survival: Log-rank (Mantel-Cox) test, *P ≤ 0.05. **(C)** Groups of aged WT mice (48–52-wk-old; n = 7) were treated and infected as depicted in B. Organs were harvested on day 4 p.i. Viral replication in upper airways was quantified as SARS-CoV-2 genome equivalents per ml by measuring expression levels of the viral gene *E* by RT-qPCR. Lung (left panel) and viral loads in lungs were determined by plaque assay on Vero E6 cells (right panel). Data from a single experiment are shown. Symbols represent individual mice and bars indicate mean ± SEM. *P ≤ 0.05, ****P ≤ 0.001, unpaired t test. **(D)** Groups of aged *Ifnar1*$^{-/-}$ mice (52–60-wk-old) were either mock-treated (n = 9) or treated therapeutically by subcutaneous injection of 3 µg IFN-γ daily for 1 wk (n = 8) starting 1 d after infection with 100 PFU MA20. Mock-treated control group is the same as depicted in Fig. 7 E. Data from a single experiment are shown. Dashed line indicates experimental endpoint due to animal welfare. Survival: Log-rank (Mantel-Cox) test, *P ≤ 0.05.

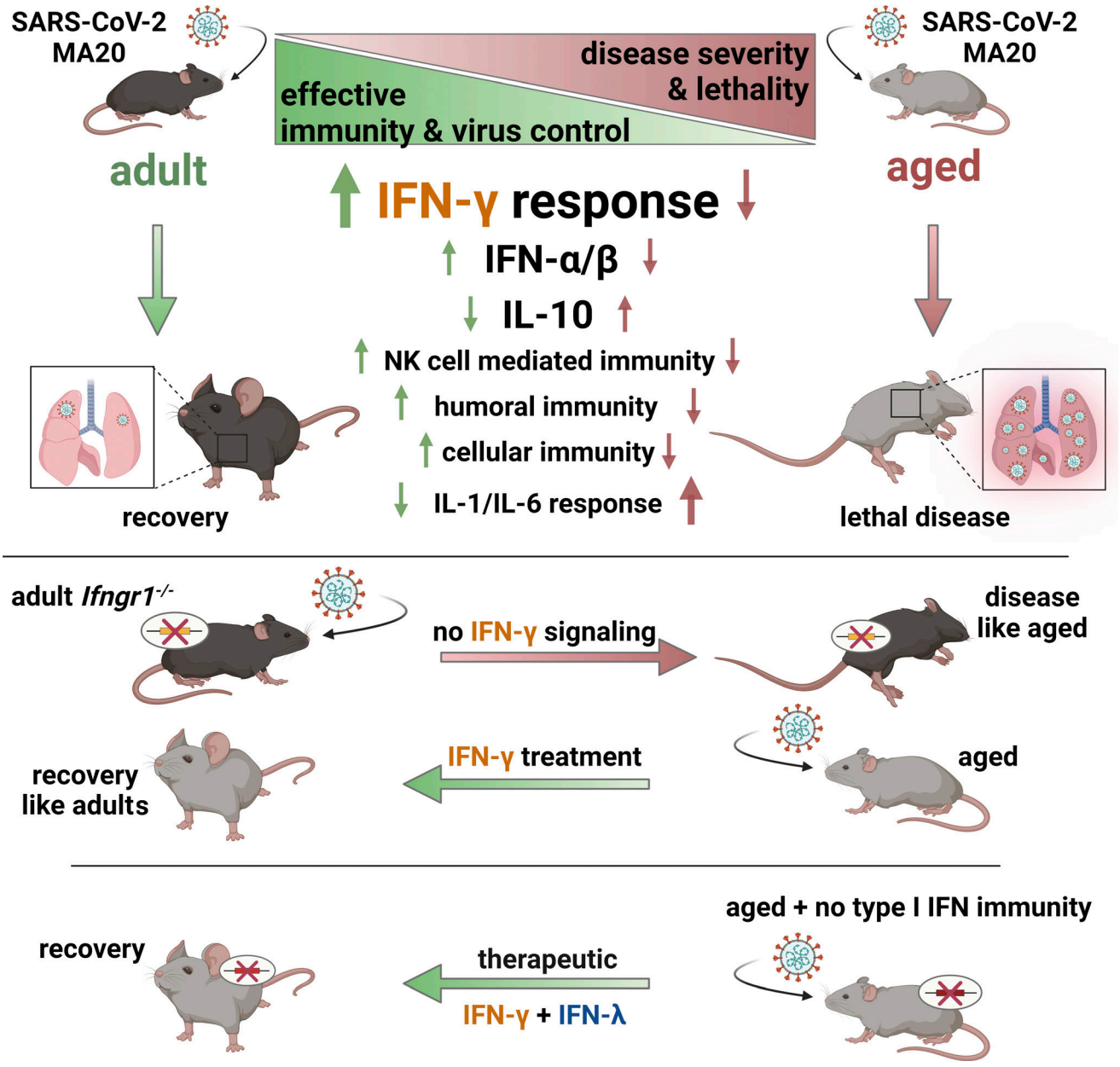

Figure S5. **Impaired immune response drives age-dependent virulence of SARS-CoV-2.** Graphical summary illustrating the age-dependent impairment of immune responses and suggested intervention strategies.

Provided online is one table. Table S1 lists histological scoring criteria.